

Article 2 :

Publié dans la revue *Mechanics Based Design of Structures and Machines*.

- **Éditeur :** Taylor & Francis
- **ISSN :** 1539-7734 **E-ISSN :** 1539-7742
- **Lien article DOI :** <https://doi.org/10.1080/15397734.2024.2418828>
- **Période de couverture par Scopus :** de 2003 à 2025
- **Domaines scientifiques :** Génie civil ; Mathématiques (Mathématiques générales)
- **Impact factor :** 3.2 (2024) ;
- **Type de source :** Revue classée A (*lien*) :
https://www.dgrstd.dz/fr/revues_A?search=Mechanics+Based+Design+of+Structures+and+Machines



The screenshot shows the homepage of the RSDT (Research Sector Development) website. At the top, there is a navigation bar with links for Accueil, DGRSDT, Activités R&D, DEV_TECH, Revues scientifiques, Services, Contact, and APPELS. The main banner features the text "Revues scientifiques de catégorie A". Below the banner, a search bar contains the query "Mechanics Based Design of Structures and Machines". The search results table has columns for TITRE DE LA REVUE, EDITEUR, ISSN, and EISSN. One result is highlighted: "MECHANICS BASED DESIGN OF STRUCTURES AND MACHINES" by TAYLOR & FRANCIS INC, with ISSN 1539-7734 and EISSN 1539-7742. To the right of the table, there is a "Télécharger" button. Below the table, there is a summary of the journal, including its cover image, volume information (Volume 53, 2025 - Issue 4), and buttons for "Submit an article" and "Journal homepage". On the left side of the page, there are metrics: 139 Views, 2 CrossRef citations to date, and 0 Altmetric. At the bottom, there is a detailed view of a research article titled "Static and free vibration response of FGM plates using higher order shear deformation theory and strain-based finite element formulation" by Taqjeddine Assas, Messaoud Bourezane, Madjda Chenafi, and Abdelouahab Tati. The article has 3044-3073 pages, was received on 07 Aug 2024, accepted on 15 Oct 2024, and published online on 27 Oct 2024. It includes links for full article, figures & data, references, citations, metrics, reprints & permissions, and a "Read this article" button.



Mechanics Based Design of Structures and Machines

An International Journal

ISSN: (Print) (Online) Journal homepage: www.tandfonline.com/journals/lmbd20

Static and free vibration response of FGM plates using higher order shear deformation theory and strain-based finite element formulation

Taqiyeddine Assas, Messaoud Bourezane, Madjda Chenafi & Abdelouahab Tati

To cite this article: Taqiyeddine Assas, Messaoud Bourezane, Madjda Chenafi & Abdelouahab Tati (27 Oct 2024): Static and free vibration response of FGM plates using higher order shear deformation theory and strain-based finite element formulation, Mechanics Based Design of Structures and Machines, DOI: [10.1080/15397734.2024.2418828](https://doi.org/10.1080/15397734.2024.2418828)

To link to this article: <https://doi.org/10.1080/15397734.2024.2418828>



Published online: 27 Oct 2024.



Submit your article to this journal 



View related articles 



CrossMark

View Crossmark data 



Static and free vibration response of FGM plates using higher order shear deformation theory and strain-based finite element formulation

Taqiyeddine Assas^a, Messaoud Bourezane^a, Madjda Chenafi^a, and Abdelouahab Tati^b

^aLaboratoire d'Aménagements Hydrauliques et Environnement (LAHE), Département de Génie Civil et Hydraulique, Université de Biskra, Biskra, Algeria; ^bLaboratoire de Génie Energétique et matériaux, Université de Biskra, Biskra, Algeria

ABSTRACT

The primary objective and novelty of this work lie in the development of a new four-node quadrilateral finite element based on strain-based high-order shear deformation theory (HSDT). This is the first study to apply this innovative approach to analyze both the static and free vibration behaviors of functionally graded (FG) plates. Another key novelty is the reduction in the number of unknowns to five, unlike other high-order shear deformation theories that employ a larger number of unknowns. This reduction is achieved by applying the condition of zero transverse shear stress at the top and bottom free surfaces of the FG plate and by assuming that the transverse shear strains are sinusoidally distributed through the thickness. The material properties of FG plates are modeled to vary according to a simple power law based on the volume fractions of their constituents. The developed finite element possesses five degrees of freedom (DOFs) per node, resulting from the combination of two strain-based elements: the first is a membrane with two DOFs, and the second is a bending plate with three DOFs. The displacement fields of the proposed element are expressed using high-order terms based on the strain approach, which satisfy compatibility equations and rigid body modes. Furthermore, the concept of the neutral surface is introduced to eliminate membrane-bending coupling. The elementary stiffness and mass matrices are derived using both the total potential energy principle and Hamilton's principle. The performance and convergence of the proposed element are validated through examples from the literature.

ARTICLE HISTORY

Received 7 August 2024
Accepted 15 October 2024

KEYWORDS

Static; free vibration;
high-order shear
deformation; functionally
graded; strain-based

1. Introduction

Functionally graded materials (FGMs) are a type of heterogeneous composite material comprising a blend of isotropic substances, typically ceramics and metals, which were first introduced by a team of Japanese scientists in 1984 (Fukui 1991). The mechanical characteristics of FGMs transition continuously and seamlessly between the surfaces, effectively avoiding the stress concentrations at the interfaces observed in laminated composites (Akavci and Tanrikulu 2015). Since their inception, FGMs have found widespread applications beyond their original use as thermal barriers in aerospace structures and are now extensively used in various structural applications. Owing to the remarkable properties of FGMs, many studies have been conducted on the static, dynamic, and buckling responses of FGM beams, plates, and shells using several numerical and analytical

methods based on various theories. These include classical plate theory (CPT), first-order shear deformation theory (FSDT) with a linear variation of displacements, and high-order shear deformation theory (HSDT), which incorporates high-order variations of displacements across the plate thickness (Nguyen et al. 2014).

Firstly, classical plate theory (CPT) has been widely employed by researchers to study thin functionally graded materials (FGMs) plates. However, this theory neglects transverse shear stress, which limits its applicability to the analysis of medium and thick plates. Timoshenko and Woinowsky-Krieger (1959) applied CPT to study both plates and shells, while Leissa (1973) investigated the natural oscillations of rectangular thin isotropic plates. Javaheri and Eslami (2002) examined the buckling characteristics of FGM plates subjected to compressive loading. Mohammadi, Saidi, and Jomehzadeh (2010) introduced an analytical solution using the Levy solution to analyze buckling phenomena in FGM plates based on CPT. Damanpack et al. (2013) proposed a purely boundary-element approach for the static analysis of thin FGM plates using CPT and the concept of the neutral surface.

Next, the Reissner-Mindlin plate theory (Mindlin 1951), also known as first-order shear deformation theory (FSDT), addresses the limitations of classical plate theory (CPT). In this model, transverse shear deformation is assumed to be constant throughout the plate thickness, allowing for the analysis of moderate and thick plates. Batra and Jin (2005) applied FSDT in conjunction with the finite element method (FEM) to investigate the free vibration response of square FGM plates. Hosseini-Hashemi et al. (2010a) proposed an analytical approach for the free vibration response of moderately thick rectangular plates supported by elastic foundations, based on FSDT. Thai and Choi (2013a, 2013b) and Thai et al. (2014) developed a simplified FSDT for FG plates, composite laminates, and sandwich FG plates. Additionally, Bellifa et al. (2016) introduced a novel FSDT to examine the bending and vibration characteristics of FG plates. Belounar et al. (2022a) proposed a finite element model using the strain approach and FSDT for the static and vibrational behavior of FG square and circular plates. In another study, Belounar, Boussem, and Tati (2022b) introduced a new quadrilateral finite element based on assumed strain and FSDT for the buckling and free vibration response of skew, circular, and square FG plates.

On the other hand, to eliminate the need for shear correction factors, the high-order shear deformation theory (HSDT) proposed by Reddy (2000) has been extensively studied by various researchers for the static, buckling, and free vibration analysis of functionally graded (FG) plates. Zenkour (2006) presented an analytical solution using sinusoidal shear deformation theory (SSDT) for the bending behavior of FG plates. Matsunaga (2008) introduced a two-dimensional (2-D) HSDT to study the characteristic frequencies and buckling stresses of FG plates. Talha and Singh (2010) conducted a comprehensive investigation of the vibrational and static responses of rectangular and square FG plates using HSDT. Hosseini-Hashemi, Fadaee, and Atashipour (2011) proposed an analytical method for the free vibratory response of square plates supported by elastic foundations based on Reddy's third-order shear deformation theory (TSĐT). Mechab, Mechab, and Benaissa (2013) suggested a refined plate theory (RPT) with four unknowns, using HSDT for the static and dynamic responses of FG plates. Mantari, Granados, and Guedes Soares (2014) employed a novel non-polynomial HSDT to examine the free vibrational analysis of FG plates supported by elastic foundations. Tati (2021b) developed a four-node, five-variable finite element based on HSDT for the bending behavior of FG plates. In another study, Tati (2021a) analyzed the buckling behavior of FG plates using his numerical solution (Tati 2021b). Sadgui and Tati (2022) presented a novel TSĐT to examine the dynamic and stability analyses of FG plates. Tati, Belounar, and Sadgui (2024) investigated the bending and free vibration analysis of FG circular plates using a five-unknowns HSDT.

Recently, the finite element method (FEM) has been recognized as a reliable and powerful computational tool for the analysis of FG structures. Many numerical models based on FEM have been developed by different researchers to accurately predict the behavior of FG structures. (Katiyar, Gupta, and Tounsi 2022; Bentrar et al. 2023; Tien et al. 2023; Mesbah et al. 2023; Xia

et al. 2023; Belabed et al. 2024a; Belabed et al. 2024b; Belabed et al. 2024c; Sekban et al. 2024; Attia et al. 2024; Lakhdar et al. 2024; Cuong et al. 2024; Meftah et al. 2024).

Additionally, recent research (Ba, Wu, and Liang 2020; Liu et al. 2022; Huang et al. 2022; Li et al. 2023; Wang et al. 2023; Zhang et al. 2023; Zhang and Zhang 2023; Yang et al. 2024; Yuan et al. 2024; Deng et al. 2024; Tian et al. 2024; Su et al. 2024) illustrates the critical role of advanced materials, innovative design methodologies, and computational techniques in addressing contemporary challenges in engineering and structural analysis.

Several workers have introduced the strain approach to produce robust and accurate finite elements. Ashwell and Sabir (1972) were the first to propose such elements, which were designed particularly for problems involving curves. Hence, this approach has been developed for plane elastic elements (Sabir 1985; Belarbi and Maalem 2005; Rebiai and Belounar 2013) and then extended to 3D elasticity problems (Belarbi and Charif 1999; Belounar and Guerraiche 2014; Messai, Belounar, and Merzouki 2019), as well as plate bending (Belounar and Guenfoud 2005; Belounar, Benmebarek, and Belounar 2020; Belounar et al. 2019; Boussem and Belounar 2020; Belounar, Benmebarek, and Belounar 2020; Boussem, Belounar, and Belounar 2022).

It is important to note that all previously formulated plate elements using the strain approach were specifically designed for isotropic materials using FSDT. This limitation has motivated the authors to develop, for the first time, a novel strain approach finite element based on HSDT for the analysis of FG plates.

This work is the first to apply the strain approach and High-Order Shear Deformation Theory (HSDT) to study the static and free vibration of square, skew, and circular FG plates by developing a new four-node quadrilateral element. Unlike other formulations of HSDT, which often require more than five variables, this approach reduces the number of unknowns to five by applying the condition of zero transverse shear stress at the upper and lower free faces of the FG plate, along with the assumption that the transverse shear strains are distributed sinusoidally throughout the thickness. The material properties of the FG plate are graded through the thickness following a simple power-law variation of the volume fractions of its components. The concept of the neutral surface is introduced to eliminate the membrane-bending coupling. The present element, called HSBQP20 (High-Order Strain-Based Quadrilateral Plate with 20 degrees of freedom), has five essential unknowns ($u, v, w, \beta_x, \beta_y$) at each of the four corner nodes, and their displacement functions are formulated by combining membrane and bending elements based on the strain approach. The membrane element, called SBRIE (Strain-Based Rectangular In-Plane Elasticity), was developed by Sabir and Sfendji (1995) and possesses two degrees of freedom (DOFs) at each node (u, v). While, the bending element, named MSBQP (Mindlin Strain Based Quadrilateral Plate), developed by Boussem, Belounar, and Belounar (2022), includes three DOFs (w, β_x, β_y) per node. The displacement field of the proposed element includes high-order terms, which are obtained from assumed strain functions that satisfy both compatibility equations and rigid body modes. Additionally, the stiffness and mass matrices are calculated using the potential energy and Hamilton's Principle. The efficacy and validity of the formulated element are confirmed by several examples drawn from the existing literature. Furthermore, the impact of various parameters, including side-to-thickness ratio (a/h), power-law index (p), aspect ratio (b/a), geometric shape, and loading type with various boundary conditions, on the plate behavior is also considered.

2. Mathematical model

2.1. Basic assumptions

The assumptions of the current theory are as follows:

- The origin of the Cartesian coordinate system is defined at the neutral surface of the functionally graded (FG) plate.

- Displacement field: the displacement field within the element is usually approximated by polynomial functions (e.g., bilinear or high-order polynomials) based on the strain approach, which satisfy both rigid body modes and compatibility equations (“see Appendix”).
- The transverse normal stress (σ_z) is negligible compared to in-plane stresses σ_x and σ_y .
- Small deformations: the displacements are small compared to the thickness of the plate and consequently strains involved are infinitesimal.
- The Poisson’s ratio (ν) of the FGM plates is assumed to be constant.

2.2. Displacement field

According to Tati (2021b) and based on the assumptions outlined in the preceding section, the displacement field can be expressed as follows:

$$\begin{aligned} u(x, y, z) &= u_0(x, y) + z\beta_x(x, y) \\ v(x, y, z) &= v_0(x, y) + z\beta_y(x, y) \\ w(x, y, z) &= w_0(x, y) + \frac{h^2}{\pi^2} \left(\cos \frac{2\pi z}{h} \right)^2 \Psi_z(x, y) \end{aligned} \quad (1)$$

where u , v , and w represent the displacements in the x , y , z directions, respectively, while u_0 and v_0 denote the displacements at the neutral surface. $w_0(x, y)$ represents the lateral displacement of neutral surface points of the plate. The variables (β_x, β_y) correspond to the normal rotations in the yz -plane and xz -plane, respectively. Additionally, Ψ_z is the transverse component of the displacement, which represents the stretching contributions. To eliminate this variable, we assume zero lateral shear stress at the upper and lower free surfaces of the FG plate, while considering that the lateral shear stresses are distributed sinusoidally throughout the thickness.

2.3. Kinematics

The relationship between strains and displacements within a plate can be expressed using the Von Kármán deformation tensor as follows:

$$\left\{ \begin{array}{l} \varepsilon_x = u_{,x}(x, y, z) = u_{0,x}(x, y) + z\beta_{x,x}(x, y) \\ \varepsilon_y = v_{,y}(x, y, z) = v_{0,y}(x, y) + z\beta_{y,y}(x, y) \\ \gamma_{xy} = u_{,y}(x, y, z) + v_{,x}(x, y, z) = u_{0,y}(x, y) + v_{0,x}(x, y) + z(\beta_{x,y}(x, y) + \beta_{y,x}(x, y)) \\ \gamma_{xz} = u_{,z}(x, y, z) + w_{,x}(x, y, z) = \beta_x(x, y) + w_{0,x}(x, y) + \frac{h^2}{\pi^2} \left(\cos \frac{2\pi z}{h} \right)^2 \Psi_{z,x}(x, y) \\ \gamma_{yz} = v_{,z}(x, y, z) + w_{,y}(x, y, z) = \beta_y(x, y) + w_{0,y}(x, y) + \frac{h^2}{\pi^2} \left(\cos \frac{2\pi z}{h} \right)^2 \Psi_{z,y}(x, y) \end{array} \right. \quad (2)$$

Equation (2) can be reformulated as follows:

$$\left\{ \begin{array}{l} \varepsilon_x = \varepsilon_x^0 + z\kappa_x \\ \varepsilon_y = \varepsilon_y^0 + z\kappa_y \\ \gamma_{xy} = \gamma_{xy}^0 + z\kappa_{xy} \\ \gamma_{xz} = \gamma_{xz}^0 + \frac{h^2}{\pi^2} \left(\cos \frac{2\pi z}{h} \right)^2 \Psi_{z,x}(x, y) \\ \gamma_{yz} = \gamma_{yz}^0 + \frac{h^2}{\pi^2} \left(\cos \frac{2\pi z}{h} \right)^2 \Psi_{z,y}(x, y) \end{array} \right. \quad (3)$$

where

$$\begin{aligned}\varepsilon_x^0 &= u_{0,x}(x, y); \varepsilon_y^0 = v_{0,y}(x, y); \gamma_{xy}^0 = u_{0,y}(x, y) + v_{0,x}(x, y) \\ \kappa_x &= \beta_{x,x}(x, y); \kappa_y = \beta_{y,y}(x, y); \kappa_{xy} = \beta_{x,y}(x, y) + \beta_{y,x}(x, y) \\ \gamma_{xz}^0 &= \beta_x(x, y) + w_{0,x}(x, y); \gamma_{yz}^0 = \beta_y(x, y) + w_{0,y}(x, y)\end{aligned}\quad (4)$$

To remove the variable $\Psi_z(x, y)$, the zero lateral shear stress condition is imposed at both the bottom and top surfaces of the plate as follows:

$$\begin{aligned}\gamma_{xz}\left(\pm\frac{h}{2}\right) &= \gamma_{yz}\left(\pm\frac{h}{2}\right) = 0 \\ \gamma_{xz}\left(\pm\frac{h}{2}\right) &= \gamma_{xz}^0 + \frac{h^2}{\pi^2}\Psi_{z,x}(x, y) = 0; \gamma_{yz}\left(\pm\frac{h}{2}\right) = \gamma_{yz}^0 + \frac{h^2}{\pi^2}\Psi_{z,y}(x, y) = 0\end{aligned}\quad (5)$$

Which lead to

$$\Psi_{z,x}(x, y) = -\frac{\pi^2}{h^2}\gamma_{xz}^0; \Psi_{z,y}(x, y) = -\frac{\pi^2}{h^2}\gamma_{yz}^0 \quad (6)$$

Using Eq. (6), the shear strain terms of Eq. (3) can be represented by:

$$\gamma_{xz} = \gamma_{xz}^0 \left(1 - \cos^2\left(\frac{2\pi z}{h}\right)\right) \quad (7a)$$

$$\gamma_{yz} = \gamma_{yz}^0 \left(1 - \cos^2\left(\frac{2\pi z}{h}\right)\right) \quad (7b)$$

Assuming an isotropic material, the shear stress can be described as:

$$\tau_{xz} = \frac{5}{6}D_{44}\gamma_{xz}^0 \quad (8a)$$

$$\tau_{yz} = \frac{5}{6}D_{55}\gamma_{yz}^0 \quad (8b)$$

where D_{44} and D_{55} are the material's elastic stiffness coefficients.

The energy per unit surface area of shear strain can be given by:

$$U_{sd}^{RM} = \frac{1}{2} \int_{-\frac{h}{2}}^{\frac{h}{2}} (\tau_{xz}\gamma_{xz}^0 + \tau_{yz}\gamma_{yz}^0) dz = \frac{1}{2} \int_{-\frac{h}{2}}^{\frac{h}{2}} \left(\frac{5}{6}D_{44}(\gamma_{xz}^0)^2 + \frac{5}{6}D_{55}(\gamma_{yz}^0)^2 \right) dz \quad (9a)$$

$$U_{sd}^{RM} = \frac{15}{26}D_{44}h \left((\gamma_{xz}^0)^2 + (\gamma_{yz}^0)^2 \right) \quad (9b)$$

For shear strain varying across thickness, using the following equations.

$$\gamma_{xz} = f(z)\gamma_{xz}^0 \quad \gamma_{yz} = f(z)\gamma_{yz}^0 \quad (10)$$

where $f(z)$ represents a shear function defined as follows:

$$f(z) = C \left(1 - \cos^2\left(\frac{2\pi z}{h}\right)\right)$$

C represents the enhancement factor. Additionally, the shear stresses are determined by:

$$\tau_{xz} = f(z)D_{44}\gamma_{xz}^0 \quad \tau_{yz} = f(z)D_{55}\gamma_{yz}^0 \quad (11)$$

The energy per unit area of the shear strain can be represented as:

$$U_{sd}^{\text{SIN}} = \frac{1}{2} \int_{-\frac{h}{2}}^{\frac{h}{2}} (\tau_{xz}\gamma_{xz} + \tau_{yz}\gamma_{yz}) dz = \frac{1}{2} D_{44} \left((\gamma_{xz}^0)^2 + (\gamma_{yz}^0)^2 \right) \int_{-\frac{h}{2}}^{\frac{h}{2}} f(z)^2 dz \quad (12)$$

Integrating the above equation over the thickness gives:

$$U_{sd}^{\text{SIN}} = \frac{1}{2} D_{44} \left((\gamma_{xz}^0)^2 + (\gamma_{yz}^0)^2 \right) \frac{3}{8} C2h \quad (13)$$

Equating the two energy expressions in Eqs. (13) and (9b) yields:

$$\frac{3}{8} C^2 h = \frac{5}{6} h$$

Then,

$$C = \frac{2\sqrt{5}}{3}$$

Therefore, the displacement field is defined using only five unknowns, derived from the high-order model proposed by Tati (2021b), as follows:

$$\begin{aligned} u(x, y, z) &= u_0(x, y, z) + z\beta_x(x, y) \\ v(x, y, z) &= v_0(x, y, z) + z\beta_y(x, y) \\ w(x, y, z) &= f(z)w_0(x, y) + (f(z) - 1)G(x, y) \end{aligned} \quad (14)$$

where $G(x, y)$ is a function defined by:

$$\beta_x(x, y) = \frac{\partial G(x, y)}{\partial x} \quad \beta_y(x, y) = \frac{\partial G(x, y)}{\partial y} \quad (15)$$

The strain vectors are expressed in the form of a matrix as follows:

$$\{\varepsilon\} = \begin{Bmatrix} \varepsilon_x \\ \varepsilon_y \\ \gamma_{xy} \end{Bmatrix} = \{\varepsilon^0\} + z\{\kappa\} = \begin{Bmatrix} \varepsilon_x^0 \\ \varepsilon_y^0 \\ \gamma_{xy}^0 \end{Bmatrix} + z \begin{Bmatrix} \kappa_x \\ \kappa_y \\ \kappa_{xy} \end{Bmatrix} \quad (16)$$

$$\{\gamma_z\} = \begin{Bmatrix} \gamma_{xz} \\ \gamma_{yz} \end{Bmatrix} = f(z) \begin{Bmatrix} \gamma_{xz}^0 \\ \gamma_{yz}^0 \end{Bmatrix} \quad (17)$$

where $f(z) = \frac{2\sqrt{5}}{3} (1 - \cos^2(\frac{2\pi z}{h}))$.

2.4. Material characteristics

This work considers a rectangular functionally graded (FG) plate with length a , width b , and thickness \square . As shown in Fig. 1, the plate is composed of metallic material on its top surface ($z = \frac{h}{2}$) and ceramic material on its bottom surface ($z = -\frac{h}{2}$). According to Praveen and Reddy (1998), the effective material characteristics, including Young's modulus E and mass density ρ , change in the thickness direction according to a power-law function, expressed as follows:

$$E(z) = E_m + (E_c - E_m) \left(\frac{z}{h} + \frac{1}{2} \right)^p \quad (18)$$

$$\rho(z) = \rho_m + (\rho_c - \rho_m) \left(\frac{z}{h} + \frac{1}{2} \right)^p \quad (19)$$

For simplicity, Poisson's ratio ν is considered to remain constant throughout the thickness, as its effect on deformation is much smaller compared to that of Young's modulus. Where, subscripts m and c denote the material characteristics of the metal and the ceramic, respectively, z represents the coordinate in the direction of the thickness ($-h/2 \leq z \leq +h/2$), and p represents the gradient index which ($p \geq 0$).

2.5. Constitutive equations

The constitutive relationships in linear form for (FG) plate can be articulated as (Belounar, Boussem, and Tati 2022b):

$$\{\sigma\} = [D_\sigma]\{\varepsilon\} \quad (20)$$

$$\begin{Bmatrix} \sigma_x \\ \sigma_y \\ \tau_{xy} \end{Bmatrix} = \begin{bmatrix} D_{11} & D_{12} & 0 \\ D_{21} & D_{22} & 0 \\ 0 & 0 & D_{66} \end{bmatrix} \begin{Bmatrix} \varepsilon_x \\ \varepsilon_y \\ \gamma_{xy} \end{Bmatrix} \quad (21)$$

$$\{\tau\} = [D_\tau]\{\gamma_z\} \quad (22)$$

$$\begin{Bmatrix} \tau_{xz} \\ \tau_{yz} \end{Bmatrix} = \begin{bmatrix} D_{44} & 0 \\ 0 & D_{55} \end{bmatrix} \begin{Bmatrix} \gamma_{xz} \\ \gamma_{yz} \end{Bmatrix} \quad (23)$$

where ($\sigma_x, \sigma_y, \tau_{xy}, \tau_{xz}, \tau_{yz}$) and ($\varepsilon_x, \varepsilon_y, \gamma_{xy}, \gamma_{xz}, \gamma_{yz}$) are the stresses and strains, respectively. The stiffness coefficients D_{ij} can be determined based on the material properties given in Eq.(18) as follows (Tati 2021b):

$$D_{11} = D_{22} = \frac{E(z)}{1 - \nu^2}; D_{12} = D_{21} = \nu D_{11}; D_{44} = D_{55} = D_{66} = \frac{E(z)}{2(1 + \nu)}$$

2.6. Neutral surface position

The asymmetrical material characteristics of FG plates relative to the mid-surface introduce a coupling effect between stretching and bending. Therefore, to avoid the complexity imposed by this effect, the resultants of force and moment are evaluated relative to the neutral surface, which

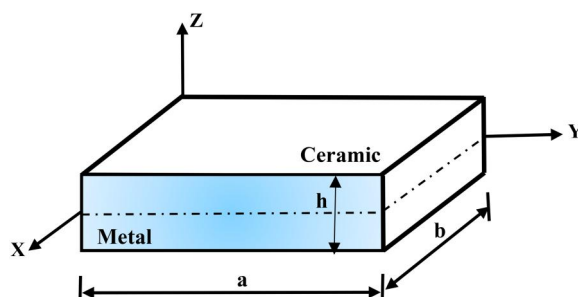


Figure 1. Geometry of rectangular FGM plate.

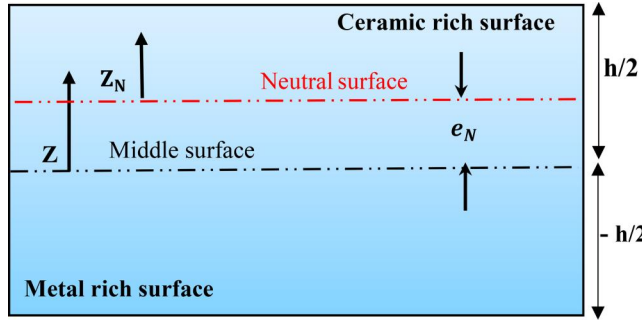


Figure 2. The location of neutral plane of FG plate.

is not aligned with the mid-plane of the plate, as indicated in Fig. 2.

$$Z_N = Z - e_N \quad (24)$$

e_N is the distance between the neutral surface and the mid-surface of the plate.

Therefore, the neutral surface's location is defined by Tati, Belounar, and Sadgui (2024):

$$e_N = \frac{\int_{-\frac{h}{2}}^{\frac{h}{2}} E(z) z dz}{\int_{-\frac{h}{2}}^{\frac{h}{2}} E(z) dz} \quad (25)$$

2.7. Stress resultants

The total in-plane forces $\{N\}$, moment resultants $\{M\}$, and shear forces $\{T\}$ are determined by integrating the stress components across the thickness h of the FGM plate as expressed by Belounar et al. (2022a):

$$\begin{Bmatrix} N_x \\ N_y \\ N_{xy} \end{Bmatrix} = \int_{-\frac{h}{2}}^{\frac{h}{2}} \begin{Bmatrix} \sigma_x(z) \\ \sigma_y(z) \\ \tau_{xy}(z) \end{Bmatrix} dz; \begin{Bmatrix} M_x \\ M_y \\ M_{xy} \end{Bmatrix} = \int_{-\frac{h}{2}}^{\frac{h}{2}} \begin{Bmatrix} \sigma_x(z) \\ \sigma_y(z) \\ \tau_{xy}(z) \end{Bmatrix} (z - e_N) dz; \begin{Bmatrix} T_x \\ T_y \end{Bmatrix} = \int_{-\frac{h}{2}}^{\frac{h}{2}} \begin{Bmatrix} \tau_{xz} \\ \tau_{yz} \end{Bmatrix} dz \quad (26)$$

The relationship between resultant stresses and strains is described as follows:

$$\begin{Bmatrix} N \\ M \\ T \end{Bmatrix} = \begin{bmatrix} [D_m] & 0 & 0 \\ 0 & [D_b] & 0 \\ 0 & 0 & [D_s] \end{bmatrix} \begin{Bmatrix} \epsilon^m \\ \kappa \\ \gamma \end{Bmatrix} \quad (27)$$

where the constitutive matrices for bending $[D_b]$, membrane $[D_m]$, and shear $[D_s]$ are given by Sadgui and Tati (2022):

$$[D_m] = \begin{bmatrix} 1 & \nu & 0 \\ \nu & 1 & 0 \\ 0 & 0 & \frac{1-\nu}{2} \end{bmatrix} \int_{-h/2}^{h/2} \frac{E(z)}{(1-\nu^2)} dz \quad (28)$$

$$[D_b] = \begin{bmatrix} 1 & \nu & 0 \\ \nu & 1 & 0 \\ 0 & 0 & \frac{1-\nu}{2} \end{bmatrix} \int_{-h/2}^{h/2} \frac{E(z)}{(1-\nu^2)} (z - e_N)^2 dz \quad (29)$$

$$[D_s] = \begin{bmatrix} 1 & 0 \\ 0 & 1 \end{bmatrix} \int_{-h/2}^{h/2} \frac{E(z)}{2(1+\nu)} (f(z))^2 dz \quad (30)$$

3. Finite element formulation

A novel quadrilateral finite element based on the strain approach and HSDT has been formulated. The element possesses 4 nodes and 5 degrees of freedom (DOFs) at each node, which include three translations (u, v, w), and two rotation angles (β_x, β_y) in the y-z and x-z planes, respectively, as shown in Fig. 3.

3.1. Displacements field of the (HSBQP20) element

To determine the displacement field for the current element (HSBQP20), we combined the displacement fields acquired from both the plate element (MSBQP) introduced by Boussem, Belounar, and Belounar (2022) and the membrane element (SBRIE) suggested by Sabir and Sfendji (1995).

First, the displacement fields obtained in Sabir and Sfendji (1995) for the membrane component (SBRIE) are:

$$\begin{Bmatrix} u \\ v \end{Bmatrix} = [P_m] \{ \alpha_m \} \quad (31)$$

where $[P_m]$ is the matrix polynomial representing the displacement functions for the membrane element and the vector of coefficients $\{ \alpha_m \} = \{ \alpha_1, \alpha_2, \dots, \alpha_8 \}^T$

$$[P_m] = \begin{bmatrix} 1 & 0 & -y & x & xy & 0 & -\frac{y^2}{2} & \frac{y}{2} \\ 0 & 1 & x & 0 & -\frac{x^2}{2} & y & xy & \frac{x}{2} \end{bmatrix} \quad (32)$$

Whereas for the plate bending component (MSBQP), the displacement functions provided by Boussem, Belounar, and Belounar (2022) are:

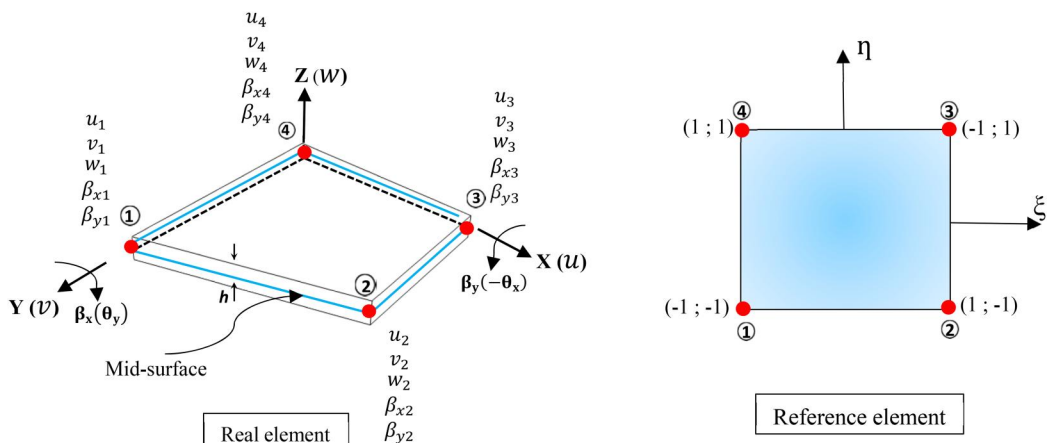


Figure 3. Quadrilateral FG plate element (HSBQP20).

$$\begin{Bmatrix} w \\ \beta_x \\ \beta_y \end{Bmatrix} = [P_b]\{\alpha_b\} \quad (33)$$

where $[P_b]$ is the matrix polynomial representing the displacement functions for the bending element and the vector of coefficients $\{\alpha_b\} = \{\alpha_9, \alpha_{10}, \dots, \alpha_{20}\}^T$

$$[P_b] = \begin{bmatrix} 1 & -x & -y & -\frac{x^2}{2} & -\left(\frac{x^2y}{2} + \frac{xy^3}{6}\right) & -\frac{y^2}{2} & -\left(\frac{xy^2}{2} + \frac{x^3y}{6}\right) & -\frac{xy}{2} & \frac{x}{2} & \frac{xy}{2} & \frac{y}{2} & \frac{xy}{2} \\ 0 & 1 & 0 & x & xy + \frac{y^3}{6} & 0 & \left(\frac{x^2y}{2} + \frac{y^2}{2}\right) & \frac{y}{2} & \frac{1}{2} & \frac{y}{2} & 0 & -\frac{y}{2} \\ 0 & 0 & 1 & 0 & \left(\frac{xy^2}{2} + \frac{x^2}{2}\right) & y & xy + \frac{x^3}{6} & \frac{x}{2} & 0 & -\frac{x}{2} & \frac{1}{2} & \frac{x}{2} \end{bmatrix} \quad (34)$$

The displacement functions obtained from Eqs. (32) and (34) have been formulated based on the strain approach, ensuring adherence to constant strains criteria, rigid body modes, and compatibility equations (see "Appendix").

As previously mentioned, combining Eqs.(32) and (34) has facilitated the derivation of interpolation functions for displacement in the formulated plate element (HSBQP20) as follows:

$$\{U_e\} = \begin{Bmatrix} u \\ v \\ w \\ \beta_x \\ \beta_y \end{Bmatrix} = \begin{bmatrix} [P_m] & [0] \\ [0] & [P_b] \end{bmatrix} \begin{Bmatrix} \{\alpha_m\} \\ \{\alpha_b\} \end{Bmatrix} = [P]\{\alpha\} \quad (35)$$

where $\{\alpha\}^T = \{\{\alpha_m\}\{\alpha_b\}\}^T = \{\alpha_1, \dots, \alpha_{20}\}^T$.

$$[P] = \begin{bmatrix} [P_m] & [0] \\ [0] & [P_b] \end{bmatrix} \quad (36)$$

The transformation matrix $[H]$, which relates the vector of elemental nodal displacements $\{\delta^e\}^T = \{\mathbf{u}_i, \mathbf{v}_i, \mathbf{w}_i, \beta_{xi}, \beta_{yi}\}_{i=1,2,3,4}$ to the vector of constants $\{\alpha\}$, can be expressed in matrix form as follows:

$$\{\delta^e\} = [H]\{\alpha\} \quad (37)$$

where

$$[H] = \{\left[P_1(x_i, y_i)\right] \left[P_2(x_i, y_i)\right] \left[P_3(x_i, y_i)\right] \left[P_4(x_i, y_i)\right]\}^T \quad (38)$$

And (x_i, y_i) are the coordinates of the four node i ($i = 1, 2, 3, 4$).

The vector of **constant parameters** $\{\alpha\}$ can be obtained from Eq. (37) as follows:

$$\{\alpha\} = [H]^{-1}\{\delta^e\} \quad (39)$$

By substituting Eq. (39) into Eq. (35) we obtain:

$$\{U_e\} = \begin{Bmatrix} u \\ v \\ w \\ \beta_x \\ \beta_y \end{Bmatrix} = [P][H]^{-1}\{\delta^e\} = [N]\{\delta^e\} \quad (40)$$

where $[N]$ is the matrix of shape functions,

$$[N] = [P][H]^{-1} \quad (41)$$

3.2. Strain-displacement relation

The strain-displacement relationships for membrane strains $\{\varepsilon^0\}$, curvatures $\{\kappa\}$ and shear strains $\{\gamma_z^0\}$, respectively are calculated using Eq. (4) as follows (Tati 2021a):

$$\{\varepsilon^0\} = \begin{Bmatrix} \varepsilon_x^0 \\ \varepsilon_y^0 \\ \gamma_{xy}^0 \end{Bmatrix} = \begin{bmatrix} \partial/\partial x & 0 \\ 0 & \partial/\partial y \\ \partial/\partial y & \partial/\partial x \end{bmatrix} \begin{Bmatrix} u \\ v \end{Bmatrix} \quad (42)$$

$$\{\kappa\} = \begin{Bmatrix} \kappa_x \\ \kappa_y \\ \kappa_{xy} \end{Bmatrix} = \begin{bmatrix} 0 & \partial/\partial x & 0 \\ 0 & 0 & \partial/\partial y \\ 0 & \partial/\partial y & \partial/\partial x \end{bmatrix} \begin{Bmatrix} w \\ \beta_x \\ \beta_y \end{Bmatrix} \quad (43)$$

$$\{\gamma_z^0\} = \begin{Bmatrix} \gamma_{xz}^0 \\ \gamma_{yz}^0 \end{Bmatrix} = \begin{bmatrix} \partial/\partial x & 1 & 0 \\ \partial/\partial y & 0 & 1 \end{bmatrix} \begin{Bmatrix} w \\ \beta_x \\ \beta_y \end{Bmatrix} \quad (44)$$

Substitution of Eq. (35) into Eqs. (42), (43) and Equation (44), we obtain:

$$\{\varepsilon^0\} = \begin{bmatrix} \partial/\partial x & 0 \\ 0 & \partial/\partial y \\ \partial/\partial y & \partial/\partial x \end{bmatrix} [[P_m][0]]_{3 \times 20} \{\alpha\} = [L_m] \{\alpha\} \quad (45)$$

$$\{\kappa\} = \begin{bmatrix} 0 & \partial/\partial x & 0 \\ 0 & 0 & \partial/\partial y \\ 0 & \partial/\partial y & \partial/\partial x \end{bmatrix} [[0][P_b]]_{3 \times 20} \{\alpha\} = [L_b] \{\alpha\} \quad (46)$$

$$\{\gamma_z^0\} = \begin{bmatrix} \partial/\partial x & 1 & 0 \\ \partial/\partial y & 0 & 1 \end{bmatrix} [[0][P_b]]_{3 \times 20} \{\alpha\} = [L_s] \{\alpha\} \quad (47)$$

where the membrane $[L_m]$, bending $[L_b]$, and the transverse shear $[L_s]$ strain matrices, respectively can be defined as follows:

$$[L_m] = \begin{bmatrix} 0 & 0 & 0 & 1 & y & 0 & 0 & 0 & 0 & 0 & 0 & 0 & 0 & 0 & 0 & 0 & 0 & 0 & 0 & 0 & 0 \\ 0 & 0 & 0 & 0 & 0 & 1 & x & 0 & 0 & 0 & 0 & 0 & 0 & 0 & 0 & 0 & 0 & 0 & 0 & 0 & 0 \\ 0 & 0 & 0 & 0 & 0 & 0 & 0 & 1 & 0 & 0 & 0 & 0 & 0 & 0 & 0 & 0 & 0 & 0 & 0 & 0 & 0 \end{bmatrix} \quad (48)$$

$$[L_b] = \begin{bmatrix} 0 & 0 & 0 & 0 & 0 & 0 & 0 & 0 & 0 & 0 & 0 & 0 & 1 & y & 0 & xy & 0 & 0 & 0 & 0 & 0 \\ 0 & 0 & 0 & 0 & 0 & 0 & 0 & 0 & 0 & 0 & 0 & 0 & 0 & 0 & 0 & 1 & x & 0 & 0 & 0 & 0 \\ 0 & 0 & 0 & 0 & 0 & 0 & 0 & 0 & 0 & 0 & 0 & 0 & 0 & 0 & 0 & 0 & (2x+y^2) & 0 & (2y+x^2) & 1 & 0 & 0 \end{bmatrix} \quad (49)$$

$$[L_s] = \begin{bmatrix} 0 & 0 & 0 & 0 & 0 & 0 & 0 & 0 & 0 & 0 & 0 & 0 & 0 & 0 & 0 & 1 & y & 0 & 0 \\ 0 & 0 & 0 & 0 & 0 & 0 & 0 & 0 & 0 & 0 & 0 & 0 & 0 & 0 & 0 & 0 & 0 & 1 & x \end{bmatrix} \quad (50)$$

The relationship between strains and displacements can be established by substituting Eq. (39) into Eqs. (45)–(47), to have:

$$\{\varepsilon^0\} = [L_m][H]^{-1}\{\delta^e\} = [\mathbf{B}_m]\{\delta^e\} \quad (51)$$

$$\{\kappa\} = [L_b][H]^{-1}\{\delta^e\} = [\mathbf{B}_b]\{\delta^e\} \quad (52)$$

$$\{\gamma_z^0\} = [L_s][H]^{-1}\{\delta^e\} = [\mathbf{B}_s]\{\delta^e\} \quad (53)$$

where $[\mathbf{B}_m]$, $[\mathbf{B}_b]$, and $[\mathbf{B}_s]$ denote the matrices of strain-displacement relationships for membrane, bending, and shear strains, respectively, as follows:

$$[\mathbf{B}_m] = [L_m][H]^{-1}; [\mathbf{B}_b] = [L_b][H]^{-1}; [\mathbf{B}_s] = [L_s][H]^{-1} \quad (54)$$

3.3. Derivation of elemental matrices

The total potential energy π of a structure can be expressed as the sum of the strain energy U and the work done by external forces W (Tati, Belounar, and Sadgui 2024):

$$\pi = U - W \quad (55)$$

where the strain energy U can be determined based on the formulations outlined by Tati (2021b):

$$U = \frac{1}{2} \int_V \left(\{\varepsilon\}^T \{\sigma\} + \{\gamma\}^T \{\tau\} \right) dV = \frac{1}{2} \int_V \left(\{\varepsilon^0\}^T \{\sigma\} + z\{\kappa\}^T \{\sigma\} + \{\gamma_z\}^T \{\tau\} \right) dV \quad (56)$$

Integrating through thickness and using Eq. (26); Eq. (56) can be expressed as follows (Sadgui and Tati 2022):

$$U = \frac{1}{2} \int_{\Omega} \left(\{\varepsilon^0\}^T \{N\} + \{\kappa\}^T \{M\} + \{\gamma_z\}^T \{T\} \right) d\Omega \quad (57)$$

Substituting Eqs. (27), (51), (52), and (53) into the preceding equation yields:

$$U = \frac{1}{2} \int_{\Omega} \left(\{\delta^e\}^T \left([\mathbf{B}_m]^T [\mathbf{D}_m] [\mathbf{B}_m] + [\mathbf{B}_b]^T [\mathbf{D}_b] [\mathbf{B}_b] + [\mathbf{B}_s]^T [\mathbf{D}_s] [\mathbf{B}_s] \right) \{\delta^e\} \right) d\Omega \quad (58)$$

where Ω and V are the top surface and the volume of the plate, respectively.

3.3.1. Bending behavior

The external work (W) done by the distributed load q_v on the FGM plate is described by Tati (2021b):

$$W = \int_{\Omega} w_0(x, y) q_v \, d\Omega \quad (59)$$

By substituting Eq. (40) in Eq. (59), we obtain:

$$W = \int_{\Omega} \{\delta^e\}^T [N]^T q_v \, d\Omega \quad (60)$$

Substitution Eqs. (58) and (60) in Eq. (55) we have:

$$\pi = \frac{1}{2} \int_{\Omega} \left(\{\delta^e\}^T ([B_m]^T [D_m] [B_m] + [B_b]^T [D_b] [B_b] + [B_s]^T [D_s] [B_s]) \{\delta^e\} \right) \, d\Omega - \int_{\Omega} \{\delta^e\}^T [N]^T q_v \, d\Omega \quad (61)$$

The canceling of the first variation of the total potential energy related to the vector of elemental nodal displacements $\{\delta^e\}$ produces the following equilibrium equation (Tati 2021b):

$$[K^e] \{\delta^e\} = \{F^e\} \quad (62)$$

where $[K^e]$ denotes the element matrix of stiffness, while $\{F^e\}$ signifies the nodal load vector for the element, expressed as (Assas, Bourezane, and Chenafi 2024):

$$[K^e] = \int \left(\underbrace{[B_m]^T [D_m] [B_m]}_{\text{Membrane}} + \underbrace{[B_b]^T [D_b] [B_b]}_{\text{Bending}} + \underbrace{[B_s]^T [D_s] [B_s]}_{\text{Shear}} \right) \, d\Omega \quad (63)$$

$$\{F^e\} = \int [N]^T q_v \, d\Omega \quad (64)$$

3.3.2. Free vibration behavior

In order to obtain the mass matrix, the Hamilton principle is used (Demir and Civalek 2017):

$$\delta \int_0^t [T - (U - W)] dt = 0 \quad (65)$$

where t is the time and T is the kinetic energy of the FGM plate, as defined by Sadgui and Tati (2022):

$$T = \frac{1}{2} \int_{-\frac{h}{2}}^{\frac{h}{2}} \rho(z) [(\dot{u})^2 + (\dot{v})^2 + (\dot{w})^2] dz \, d\Omega \quad (66)$$

Substituting Eq. (1) into the aforementioned equation, we obtain:

$$T = \frac{1}{2} \int_{\Omega} \left(I_0 ((\dot{u}_0)^2 + (\dot{v}_0)^2 + (\dot{w}_0)^2) + I_2 \left((\dot{\beta}_x)^2 + (\dot{\beta}_y)^2 \right) \right) \, d\Omega \quad (67)$$

Where the terms I_0 , I_2 and $\rho(z)$ represent the moments of inertia and mass density, respectively, which can be defined as (Sadgui and Tati 2022):

$$(I_0, I_2) = \int_{-\frac{h}{2}}^{\frac{h}{2}} \left(\left(1, (z - e_N)^2 \right) \rho(z) \right) dz \quad (68)$$

In free vibrational response, where the work produced by the externally applied forces (W) is ignored, the principal Hamiltonian Eq. (65) yields the dynamic equation of equilibrium for a system (Belounar, Boussem, and Tati 2022b):

$$[K^e]\{\delta^e\} + [M^e]\{\ddot{\delta}^e\} = 0 \quad (69)$$

$$([K^e] - \omega^2[M^e])\{\delta^e\} = 0 \quad (70)$$

where ω is the natural frequency, $[M^e]$ is the element mass matrix expressed as follows (Tati, Belounar, and Sadgui 2024):

$$[M^e] = \int_{\Omega} [N]^T [I] [N] d\Omega \quad (71)$$

$[I]$ is the inertial matrix, which is described as follows:

$$[I] = \begin{bmatrix} I_0 & 0 & 0 & 0 & 0 \\ 0 & I_0 & 0 & 0 & 0 \\ 0 & 0 & I_0 & 0 & 0 \\ 0 & 0 & 0 & I_2 & 0 \\ 0 & 0 & 0 & 0 & I_2 \end{bmatrix} \quad (72)$$

The matrices $[K^e]$ and $[M^e]$, as provided in Eqs. (63) and (71) respectively, and the equivalent nodal load vector $\{F^e\}$ from Eq. (64), are assembled to obtain the stiffnesses, mass matrices, and load vector of the structure ($[K]$, $[M]$, $\{F\}$).

For static and free vibration behavior, we apply (Belounar et al. 2022a):

$$[K]\{\delta^e\} = \{F\} \quad (73)$$

$$([K] - \omega^2[M])\{\delta^e\} = 0 \quad (74)$$

4. Results and discussion

In this section, we examine static and free vibrational analyses of FG square, skew, and circular plates using the suggested element, and their results are verified and compared with the published results in the literature. To show the efficiency and accuracy of the HSBQP20 element, a series of applications have been executed for various types of FGM plates, and considered two kinds of boundary conditions:

Clamped (CCCC)

$u = v = w = \beta_x = \beta_y = 0$ at $x = 0, a$; and $y = 0, b$.

Simply supported (SSSS)

$u = \beta_x = 1; v = w = \beta_y = 0$ at $x = 0, a$

$v = \beta_y = 1; u = w = \beta_x = 0$ at $y = 0, b$

The characteristics of the materials selected are as follows:

Material 1: Aluminum/Alumina (Al/Al₂O₃)

Material 2: Aluminum/ Zirconia-1 (ZrO₂-1)

Al₂O₃: $E_{Al2O3} = 380$ Gpa; $\rho_{Al2O3} = 3800$ Kg/m³; $\nu = 0.3$

Al: $E_{Al} = 70$ Gpa; $\rho_{Al} = 2707$ Kg/m³; $\nu = 0.3$

ZrO₂ - 1 : $E_{ZrO2-1} = 151$ Gpa; $\rho_{ZrO2-1} = 3000$ Kg/m³; $\nu = 0.3$

The results are expressed in non-dimensional parameters, which are calculated according to the equations below:

$$\bar{w} = \frac{10h^3 E_c}{a^4 q_0} w\left(\frac{a}{2}, \frac{b}{2}\right); \bar{\sigma}_x = \frac{h}{aq_0} \sigma_x\left(\frac{a}{2}, \frac{b}{2}, z\right); \bar{\sigma}_y = \frac{h}{aq_0} \sigma_y\left(\frac{a}{2}, \frac{b}{2}, z\right);$$

$$\bar{\tau}_{xy} = \frac{h}{aq_0} \tau_{xy}(0, 0, z); \bar{\tau}_{xz} = \frac{h}{aq_0} \tau_{xy}\left(0, \frac{b}{2}, z\right); \bar{\tau}_{yz} = \frac{h}{aq_0} \tau_{xy}\left(\frac{a}{2}, 0, z\right);$$

$$\bar{\beta} = \omega h \sqrt{\frac{\rho_m}{E_m}}; \bar{\omega} = \omega \frac{a^2}{h} \sqrt{\frac{\rho_c}{E_c}}; \bar{\omega} = 100 \omega h \sqrt{\frac{\rho_c}{E_c}}$$

4.1. Static analyses

The efficiency and performance of the proposed quadrilateral element for analyzing the static behavior of simply supported functionally graded (FG) square plates have been validated through various numerical examples. Both uniform and sinusoidal loading distributions are considered, and the results were compared with existing numerical and analytical solutions. The constituent materials of the FG plates in this study are metal (aluminum) and ceramic (alumina). The plates are subjected to a distributed load (x), as shown in Fig. 4, which is given by:

$$\text{Uniformly distributed load (UDL)} : q(x, y) = q_0$$

$$\text{Sinusoidally distributed load (SDL)} : q(x, y) = q_0 \sin \frac{\pi x}{a} \sin \frac{\pi y}{b}$$

In this first example, a simply supported Al/Al₂O₃ square plate with a length-to-thickness ratio of $a/h=10$ is analyzed. The dimensionless displacement and stresses of the HSBQP20 element for the FGM plates under sinusoidal distributed load (SDL) and uniform distributed load (UDL), as shown in Fig. 4, are presented in Tables 1 and 2, respectively. These results are obtained using four mesh sizes (8×8 , 12×12 , 16×16 , and 20×20) for different values of the power-law index (p), and are compared with results derived analytically using the Refined Plate Theory (RPT) of Do, Pham, and Nguyen (2020), the semi-analytical numerical model by Ye et al. (2021), an analytical solution by Zenkour (2006) using SSDT, and the numerical solutions based on HSDT by Tati (2021b). As seen in Tables 1 and 2, the results of this study are generally in good agreement with those reported in the aforementioned references across all gradient index values. Furthermore, Table 2 illustrates the influence of the power-law index (p) on the plate behavior. Indeed, it can be seen that the dimensionless displacement (\bar{w}) and the dimensionless normal stress ($\bar{\sigma}_x$) increase with increasing p , whereas the in-plane shear stress ($\bar{\tau}_{xy}$) decreases within the

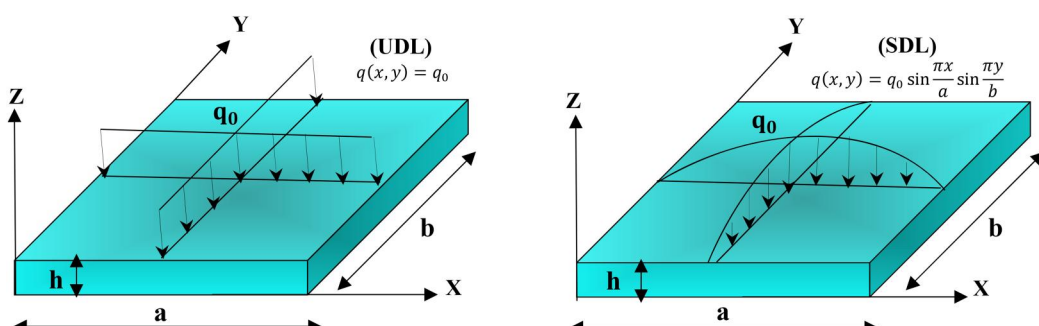


Figure 4. Square FG plates subject to uniform and sinusoidal loading distributions.

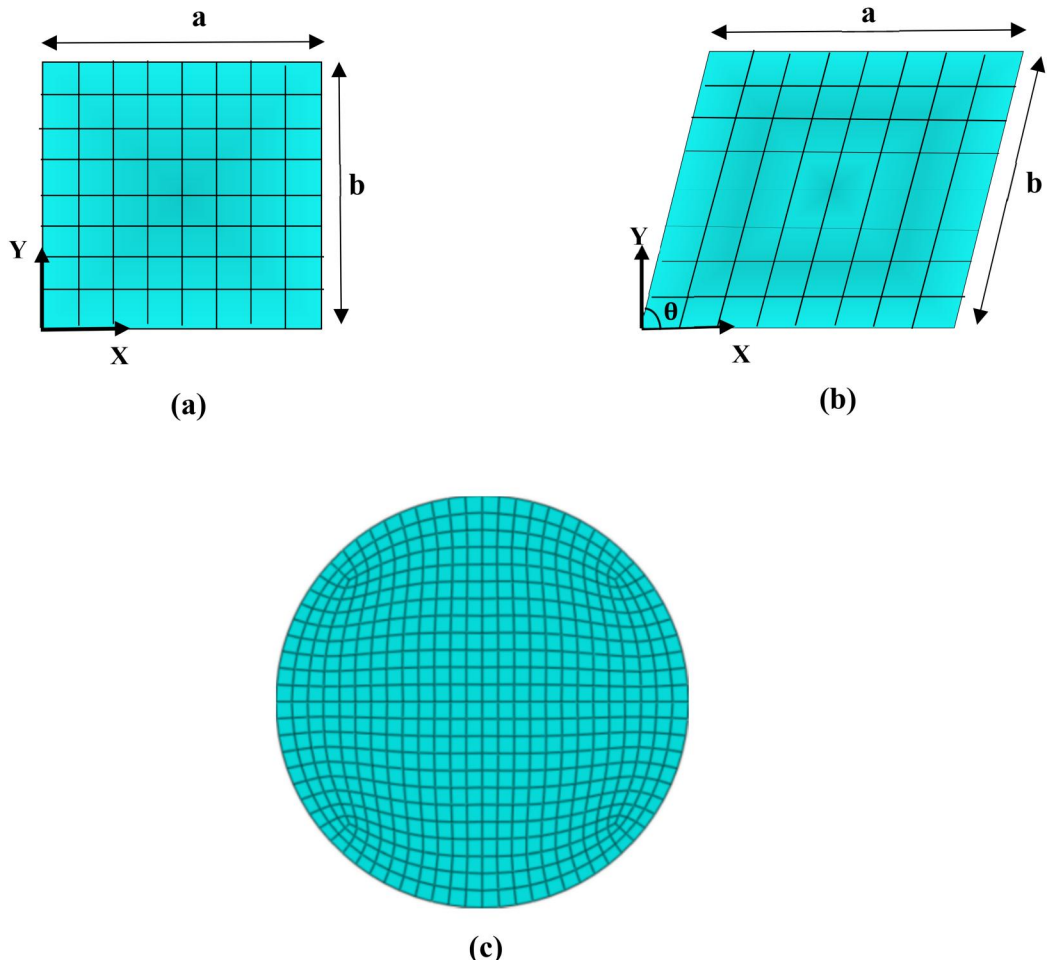


Figure 5. (a), (b) Square and skew plates with a $N \times N$ mesh of elements, (c) Circular plate with 588 quadrilateral elements.

power-law index range of 0 to 2 before increasing again as the power-law index (p) increases. Notably, for $p = 0$ and $p = 1$, the transverse shear stress ($\bar{\tau}_{xz}$) remains the same, decreases up to $p = 4$, and then increases as the plate becomes more metallic.

Figures 6–8 display the variation of the dimensionless normal stress ($\bar{\sigma}_x$), in-plane shear stress ($\bar{\tau}_{xy}$), and transverse shear stress ($\bar{\tau}_{xz}$), respectively, across the thickness for different power-law index values p of a simply supported FG square plate subjected to UDL. It can be observed that the stresses in the fully ceramic plate ($p = 0$) and the fully metallic plate ($p = \infty$) are identical. This is because the stresses in these two conditions are independent of Young's modulus and the plate is completely homogeneous.

Additionally, Figs. 6 and 7 reveal that the dimensionless normal stress ($\bar{\sigma}_x$) and the in-plane shear stress ($\bar{\tau}_{xy}$) exhibit nearly linear distributions across the thickness for isotropic plates ($p = 0$ and $p = \infty$). However, for graded plates, these stress distributions become nonlinear as the gradient index p varies through the thickness.

Figure 6 illustrates that the dimensionless normal stress ($\bar{\sigma}_x$) is tensile at the upper surface and compressive at the lower surface of the FG square plate. For $p = 0$, the stress distribution is a standard linear function, with the neutral plane located at $z/h = 0$. The maximum compressive stresses occur at the lower edge of the plate, while the maximum tensile stresses are found at the upper edge. In contrast, the in-plane shear stress ($\bar{\tau}_{xy}$) is tensile at the lower surface and

Table 1. Dimensionless displacement (\bar{w}) and stresses of FG square plates under (SDL) for different power-law index p .

p	Mesh size	Present 8×8	Present 12×12	Present 16×16	Present 20×20	(Tati 2021b)	(Do, Pham, and Nguyen 2020)	(Zenkour 2006)
0 (Ceramic)	w	0.2935	0.2950	0.2955	0.2959	0.2957	0.2961	0.2960
	σ_x	2.4294	2.1003	2.0053	1.9960	1.9570	1.9943	1.9955
	σ_y	1.5330	1.4302	1.3375	1.3125	1.3050	1.3124	1.3121
	τ_{xy}	0.6940	0.6960	0.6995	0.7030	0.7025	0.7067	0.7065
	τ_{xz}	0.2305	0.2325	0.2360	0.2390	0.2368	0.2387	0.2462
	τ_{yz}	0.2027	0.2048	0.2083	0.2113	0.2105	0.2122	0.2132
1	w	0.5573	0.5738	0.5794	0.5820	0.5882	0.5870	0.5889
	σ_x	3.7067	3.3556	3.1135	3.0545	3.0240	3.0533	3.0870
	σ_y	1.8667	1.6448	1.5261	1.4834	1.4820	1.4856	1.4894
	τ_{xy}	0.5993	0.6013	0.6048	0.6083	0.6066	0.6148	0.6110
	τ_{xz}	0.2305	0.2325	0.2360	0.2390	0.2368	0.2212	0.2462
	τ_{yz}	0.2494	0.2515	0.2550	0.2580	0.2588	0.2418	0.2622
2	w	0.7141	0.7353	0.7425	0.7458	0.7575	0.7529	0.7573
	σ_x	4.4450	3.9168	3.6344	3.4614	3.5320	3.5585	3.6094
	σ_y	1.7523	1.5441	1.4327	1.3946	1.3920	1.3935	1.3954
	τ_{xy}	0.5365	0.5385	0.5420	0.5455	0.5406	0.5493	0.5441
	τ_{xz}	0.2180	0.2200	0.2235	0.2266	0.2202	0.1892	0.2265
	τ_{yz}	0.2682	0.2703	0.2738	0.2768	0.2758	0.2369	0.2763
4	w	0.8523	0.8660	0.8773	0.8780	0.8832	0.8731	0.8819
	σ_x	4.4015	4.110	3.9927	3.9723	3.9720	3.9984	4.0693
	σ_y	1.3560	1.2536	1.2169	1.1777	1.1810	1.1794	1.1783
	τ_{xy}	0.5552	0.5578	0.5660	0.5680	0.5639	0.5740	0.5667
	τ_{xz}	0.1967	0.1987	0.2005	0.2032	0.1979	0.1596	0.2029
	τ_{yz}	0.2505	0.2530	0.2565	0.2585	0.2584	0.2083	0.2580
10	w	0.9258	0.9524	0.9614	0.9956	1.0125	1.0020	1.0089
	σ_x	6.1817	5.4583	5.0741	4.9388	4.9690	5.0142	5.0890
	σ_y	1.0973	0.9689	0.9007	0.8790	0.8822	0.8797	0.8775
	τ_{xy}	0.5797	0.5817	0.5852	0.5887	0.5868	0.5964	0.5894
	τ_{xz}	0.2090	0.211	0.2145	0.2190	0.2167	0.1858	0.2198
	τ_{yz}	0.1982	0.2003	0.2038	0.2069	0.2065	0.1770	0.2041
∞ (Metal)	w	1.5067	1.5507	1.5656	1.5725	/	1.6072	1.6070
	σ_x	2.4294	2.1003	2.0053	1.9960	/	1.9943	1.9955
	σ_y	1.5330	1.4302	1.3375	1.3125	/	1.3124	1.3121
	τ_{xy}	0.6940	0.6960	0.6995	0.7030	/	0.7067	0.7065
	τ_{xz}	0.2305	0.2325	0.2360	0.2390	/	0.2387	0.2462
	τ_{yz}	0.2027	0.2048	0.2083	0.2113	/	0.2122	0.2132

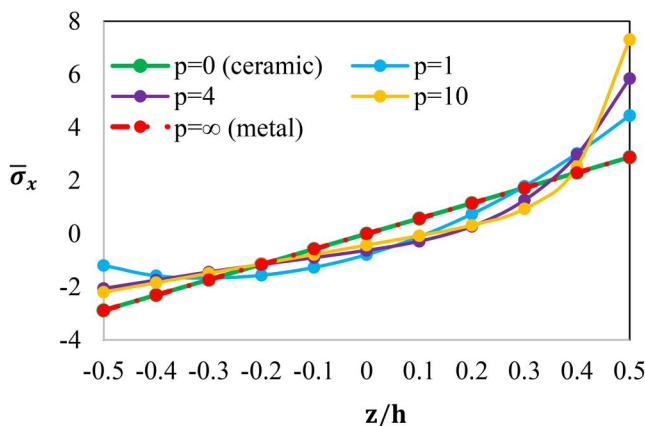
compressive at the upper surface. For the homogeneous plate, the maximum tensile shear stress is observed at the lower surface, while the minimum compressive shear stress is at the upper surface, as shown in Fig. 7.

Figure 8 illustrates the distribution of transverse shear stress ($\bar{\tau}_{xz}$) through the thickness of the plate. It can be observed that the plate is free of shear strains and stresses at both the upper and lower surfaces. For homogeneous plates ($p = 0$ and $p = \infty$), the transverse shear stress ($\bar{\tau}_{xz}$) follows a symmetric, sinusoidal distribution through the thickness, with the maximum value located at the mid-plane of the plate. However, in the case of FG plates, the distribution is not perfectly sinusoidal and does not have its maximum at the mid-plane. Additionally, for $p = 1$ and $p = 4$, the distribution becomes asymmetrical, with the maximum stress values located at $z/h = 0.1$ and $z/h = 0.3$, respectively.

In the second example, thin and thick simply supported Al/Al₂O₃ square plates are analyzed. The dimensionless displacements and stresses of the FGM plates for different values of the side-to-thickness ratio (a/h) are presented in Table 3 using a 20×20 mesh with $p = 0$. The results obtained using the present element show good agreement with those reported by Tati (2021b), Zenkour (2006), and Reddy (2000) for all cases, from thinner to thicker plates. Furthermore, the effects of several parameters, such as the power-law index (p) and the side-to-thickness ratio

Table 2. Dimensionless displacement (\bar{w}) and stresses of FG square plates under (UDL) for different power-law index p .

p	Mesh size	Present 8 × 8	Present 12 × 12	Present 16 × 16	Present 20 × 20	(Tati 2021b)	(Wenbin Ye et al. 2021)	(Do, Pham, and Nguyen 2020)
0 (Ceramic)	w	0.4638	0.4653	0.4659	0.4661	0.4663	0.4662	0.4666
	σ_x	2.8753	2.8737	2.8736	2.8735	2.8656	2.8249	2.8917
	σ_y	1.9169	1.9158	1.9157	1.9156	1.904	1.8870	1.9107
	τ_{xy}	1.2752	1.2883	1.2931	1.2954	1.266	1.2759	1.2771
	τ_{xz}	0.4265	0.4489	0.4632	0.4798	0.4696	0.4966	0.5059
	τ_{yz}	0.3790	0.4019	0.4138	0.4212	0.4174	0.4980	0.4497
1	w	0.9230	0.9263	0.9274	0.9279	0.9283	0.9212	0.9260
	σ_x	4.4435	4.4413	4.4413	4.4412	4.415	4.4030	4.4403
	σ_y	2.1781	2.1770	2.1770	2.1769	2.164	2.1572	2.1655
	τ_{xy}	1.1010	1.1125	1.1167	1.1187	1.093	1.1061	1.1417
	τ_{xz}	0.4265	0.4489	0.4632	0.4798	0.4696	0.4882	0.4688
	τ_{yz}	0.4657	0.4941	0.5088	0.5180	0.5133	0.5418	0.5124
2	w	1.1850	1.1891	1.1905	1.1912	1.1948	1.1956	1.1875
	σ_x	5.1885	5.1858	5.1858	5.1856	5.155	5.2970	5.1781
	σ_y	2.0454	2.0444	2.0443	2.0443	2.032	1.9784	2.0320
	τ_{xy}	0.9813	0.9915	0.9952	0.9970	0.9745	0.9708	1.0290
	τ_{xz}	0.4056	0.4268	0.4421	0.4569	0.4368	0.4479	0.4010
	τ_{yz}	0.4673	0.4957	0.5105	0.5197	0.5469	0.5413	0.5021
4	w	1.3738	1.3784	1.3799	1.3807	1.3916	1.3779	1.3762
	σ_x	5.8358	5.8325	5.8322	5.8320	5.797	5.9532	5.8199
	σ_y	1.7351	1.7341	1.7340	1.7340	1.724	1.7204	1.7210
	τ_{xy}	1.0237	1.0342	1.0381	1.0399	1.016	1.0335	1.0827
	τ_{xz}	0.3754	0.3921	0.4158	0.4285	0.3926	0.4187	0.3382
	τ_{yz}	0.4058	0.4303	0.4431	0.4510	0.5124	0.5105	0.4414
10	w	1.5776	1.5824	1.5841	1.5849	1.5934	1.5604	1.5774
	σ_x	7.3026	7.2980	7.2972	7.2968	7.253	7.2217	7.2931
	σ_y	1.2963	1.2955	1.2954	1.2953	1.288	1.2203	1.2843
	τ_{xy}	1.0660	1.0767	1.0806	1.0825	1.058	1.1056	1.1187
	τ_{xz}	0.4010	0.4231	0.4489	0.4555	0.4536	0.4298	0.4487
	τ_{yz}	0.3461	0.3667	0.3776	0.3843	0.4096	0.4207	0.3752
∞ (Metal)	w	2.4996	2.5049	2.5104	2.5221	/	/	2.5329
	σ_x	2.8753	2.8737	2.8736	2.8735	/	/	2.8917
	σ_y	1.9169	1.9158	1.9157	1.9156	/	/	1.9107
	τ_{xy}	1.2752	1.2883	1.2931	1.2954	/	/	1.2771
	τ_{xz}	0.4265	0.4489	0.4632	0.4798	/	/	0.5059
	τ_{yz}	0.3790	0.4019	0.4138	0.4212	/	/	0.4497

**Figure 6.** Variation of in-plane dimensional stress ($\bar{\sigma}_x$) of a square FG plate subjected to UDL with varying gradient index (p).

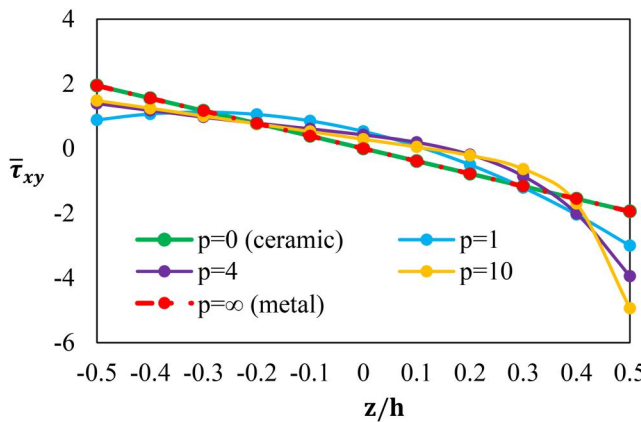


Figure 7. Variation of in-plane dimensionless shear stress ($\bar{\tau}_{xy}$) of a square FG plate subjected to UDL with varying gradient index (p).

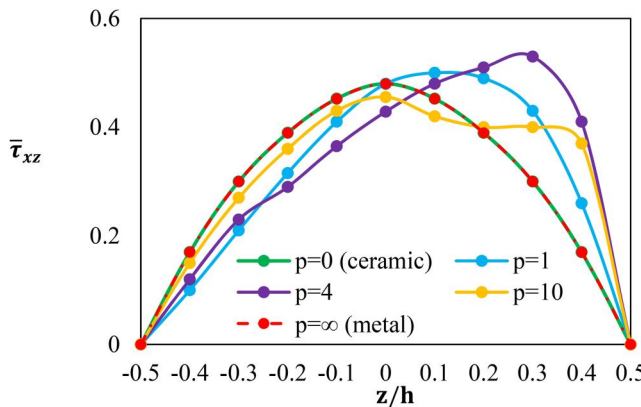


Figure 8. Variation of dimensionless lateral shear stress ($\bar{\tau}_{xz}$) of a square FG plate subjected to UDL with varying gradient index (p).

Table 3. Dimensionless displacement (\bar{w}) and stresses of FG square plates with various aspect ratios (a/h).

a/h	Theory	w	σ_x	σ_y	τ_{xy}	τ_{xz}	τ_{yz}
4	Present (20 × 20)	0.5870	1.1495	0.7664	0.5188	0.4797	0.4213
	HSDT (Tati 2021b)	0.5872	1.1425	0.7617	0.5070	0.4695	0.4173
	SSDT (Zenkour 2006)	0.5865	1.1988	0.7534	0.4906	0.4906	0.4307
	TSDT (Reddy 2000)	0.5868	1.1959	0.7541	0.4913	0.4913	0.4304
10	Present (20 × 20)	0.4661	2.8735	1.9156	1.2954	0.4798	0.4212
	HSDT (Tati 2021b)	0.4663	2.8560	1.9040	1.2660	0.4700	0.4174
	SSDT (Zenkour 2006)	0.4665	2.8932	1.9103	1.2850	0.5114	0.4429
	TSDT (Reddy 2000)	0.4666	2.8920	1.9106	1.2855	0.4963	0.4411
100	Present (20 × 20)	0.4429	28.7094	19.1396	12.9360	0.4796	0.4213
	HSDT (Tati 2021b)	0.4435	28.5600	19.0400	12.6500	0.4696	0.4174
	SSDT (Zenkour 2006)	0.4438	28.7342	19.1543	13.0125	0.5164	0.4472
	TSDT (Reddy 2000)	0.4438	28.7341	19.1543	12.9885	0.5004	0.4448

(a/h), on the bending behavior of FG plates have also been analyzed. The results are shown in Figs. 9–11.

Figure 9 shows the variation of the power-law index (p) and the side-to-thickness ratio (a/h) versus the dimensionless central deflection. It can be observed that the dimensionless central deflection decreases as the side-to-thickness ratio (a/h) increases, while it increases as the power-

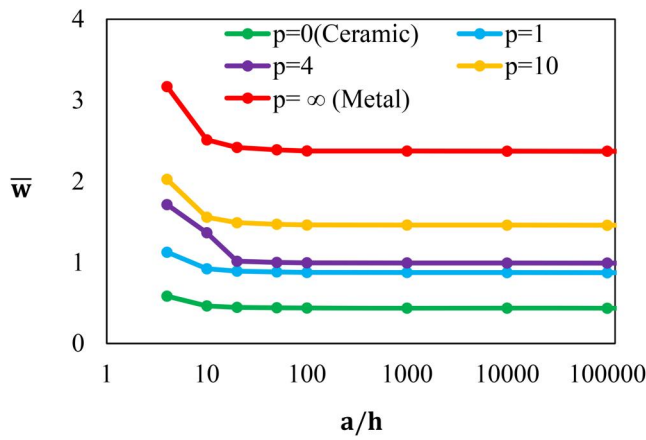


Figure 9. Variations of dimensionless displacement (\bar{w}) of an FG square plate under UDL with varying aspect ratios (a/h)

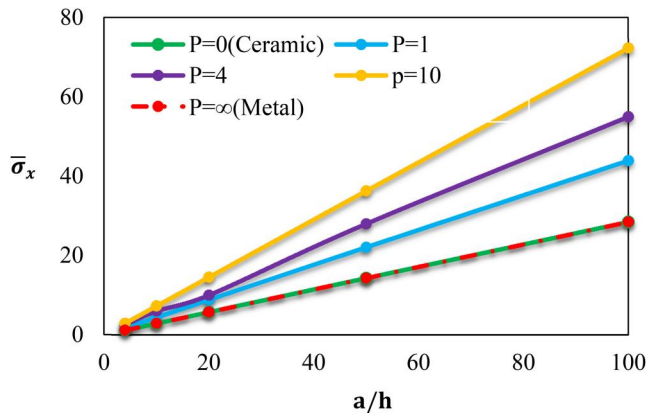


Figure 10. Change in dimensionless in-plane stress ($\bar{\sigma}_x$) of a square FG plate subjected to UDL with varying aspect ratios (a/h).

law index (p) increases. This increase occurs because a greater power-law index raises the volume fraction of metal, reducing the bending stiffness of the functionally graded (FG) plates and making them more flexible, resulting in higher deflections. In addition, the present element demonstrates robustness against shear locking and provides stable performance over a range of length-to-thickness ratios in thin plates.

As illustrated in Fig. 10, the dimensionless normal stress ($\bar{\sigma}_x$) grows as the side-to-thickness ratio (a/h) increases and reduces as the gradient index (p) decreases.

Figure 11 depicts the change in dimensionless in-plane shear stress ($\bar{\tau}_{xy}$) for various side to thickness ratios (a/h) and power law indices (p). The figure demonstrates that the dimensionless in-plane shear stress ($\bar{\tau}_{xy}$) increases with increasing aspect ratio (a/h). In addition, it reduces as the power-law index (p) varies between 0 and 2, and then increases with a greater power-law index (p). This behavior is caused by the reduction in plate stiffness, which influences the shear stress response.

4.2. Free vibration

In this subsection, the convergence of the current element (HSBQP20) has also been checked for the free vibration responses for different types of FG plates, and the findings are compared with available numerical and analytical methods.

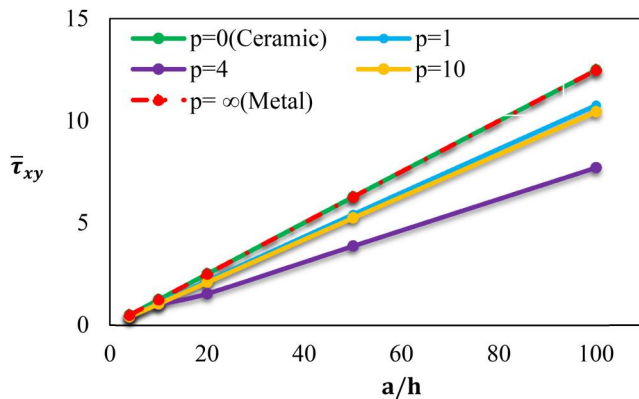


Figure 11. Change in dimensionless in-plane shear stress ($\bar{\tau}_{xy}$) of a square FG plate subjected to UDL with varying aspect ratios (a/h).

Table 4. Dimensionless natural frequencies ($\bar{\beta}$) of Al/Al₂O₃ rectangular plates.

b/a	a/h	p	Theory			
			Present	(Mantari, Granados, and Guedes Soares 2014)	(Sadgui and Tati 2022)	(Jin et al. 2014)
1	10	0	0.1133	0.1134	0.1136	0.1135
		1	0.0868	0.0868	0.0870	0.0870
		2	0.0788	0.0788	0.0788	0.0789
		5	0.0741	0.0740	0.0738	0.0741
		5	0.4150	0.4151	0.4156	0.4169
	5	0	0.3204	0.3205	0.3210	0.3222
		1	0.2897	0.2892	0.2883	0.2905
		2	0.2686	0.2666	0.2632	0.2676
		5	1.8218	1.8277	1.8224	1.8470
	2	0	1.4422	1.4460	1.4435	1.4687
		1	1.2930	1.2896	1.2675	1.3095
		2	1.1508	1.1312	1.0829	1.1450
		5	0.0716	0.0717	0.0722	0.0719
	2	0	0.0547	0.0549	0.0553	0.0550
		1	0.0498	0.0498	0.0501	0.0499
		2	0.0473	0.0470	0.0742	0.0471
		5	0.2714	0.2705	0.2721	0.2713
		5	0.2085	0.2081	0.2094	0.2088
	5	0	0.1886	0.1882	0.1888	0.1888
		1	0.1755	0.1750	0.1743	0.1754
		2	1.2915	1.2910	1.2943	0.9570
		5	1.0147	1.0137	1.0172	0.7937
	2	0	0.9050	0.9067	0.8988	0.7149
		5	0.8074	0.8064	0.7824	0.6168

4.2.1. Square plates

The free vibration of a simply supported Al/Al₂O₃ rectangular plate is analyzed. The dimensionless natural frequencies ($\bar{\beta}$) are derived using the current formulation and compared to the quasi-3D solutions from Jin et al. (2014), the high-order shear theory results of Sadgui and Tati (2022), and those of Mantari, Granados, and Guedes Soares (2014). The obtained results are presented in Table 4, using a mesh of (20 × 20) and for various values of the power-law index (p), the side-to-thickness ratio (a/h), and the aspect ratio (b/a). According to Table 4, it can be concluded that the current results are in excellent agreement with the aforementioned references. Furthermore, they are similar to the results obtained by Mantari, Granados, and Guedes Soares (2014). Additionally, it can be seen that the dimensionless natural frequencies ($\bar{\beta}$) decrease as the power

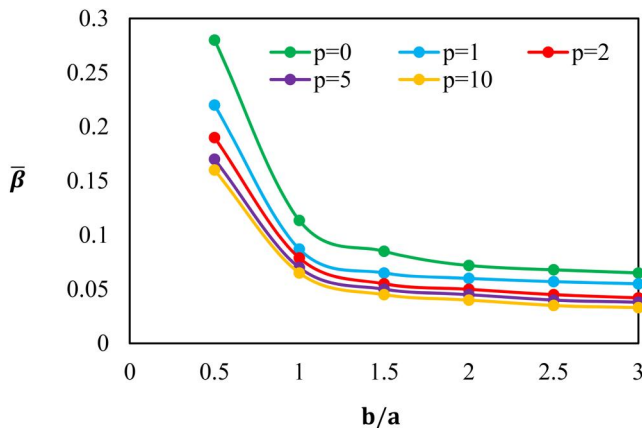


Figure 12. The effect of aspect ratio (b/a) on the dimensionless natural frequencies ($\bar{\beta}$) of $\text{Al}/\text{Al}_2\text{O}_3$ rectangular plates ($a/h = 10$).

Table 5. The first three dimensionless natural frequencies ($\bar{\omega}$) for both simply supported (SSSS) and clamped (CCCC) skew $\text{Al}/\text{ZrO}_2\text{-1}$ plate with ($a/h = 10$, $\theta = 45^\circ$).

p	Mode	Simply supported (SSSS)			Clamped (CCCC)		
		Present (16×16)	(Katili et al. 2021)	(Zhao, Lee, and Liew 2009)	Present (16×16)	(Katili et al. 2021)	(Zhao, Lee, and Liew 2009)
0	1	9.556	9.461	9.6709	16.713	16.785	16.635
	2	17.801	17.638	17.964	25.316	25.438	25.275
	3	25.794	25.364	24.985	33.406	33.616	33.377
0.5	1	8.662	8.593	8.7115	15.102	15.183	15.047
	2	16.083	15.965	16.202	22.957	23.053	22.902
	3	22.987	22.98	23.014	30.385	30.497	30.274
1	1	8.275	8.248	8.3025	14.403	14.468	14.338
	2	15.345	15.254	15.437	21.843	21.961	21.816
	3	21.928	21.949	21.907	28.940	29.048	28.833
3	1	7.861	7.839	7.884	13.584	13.646	13.523
	2	14.534	14.447	14.622	20.577	20.645	20.509
	3	20.399	20.742	20.056	27.154	27.254	27.054

index (p) increases. This occurs because a higher power-law index leads to an increased volume fraction of metal, which in turn reduces the bending stiffness of the FG plate, ultimately resulting to lower vibrational responses. It can also be observed that, for a particular power-law index p , the dimensionless natural frequencies decreases as the aspect ratio b/a increases, as shown in Fig. 12. This is due to the fact that as the aspect ratio increases, the plate becomes wider relative to its thickness, which reduces its bending stiffness and effective resisting moment. This makes the plate less capable of resisting bending, leading to lower natural frequencies. In addition, a higher aspect ratio spreads the mass over a larger area, which affects the inertial properties and reduces the vibrational energy required for motion, further lowering the natural frequencies.

4.2.2. Skew plates

Skew plates are extensively utilized in various engineering disciplines, such as aeronautical, civil, marine, and mechanical engineering. Morley (1963) conducted the original study on this type of plate. Several numerical approaches have been suggested for the effective study of skew plates due to the complexity of analytical methods.

Table 5 displays the dimensionless natural frequencies ($\bar{\omega}$) of the first three modes for SSSS and CCCC skew plates made from Material 2, with the skew angle fixed at ($\theta = 45^\circ$) and the aspect ratio ($a/h = 10$). The analysis utilized a 16×16 mesh (see Fig. 5(b)) with a gradient value p ranging from 0 to 3. The results show good agreement with those obtained from the Q4cs

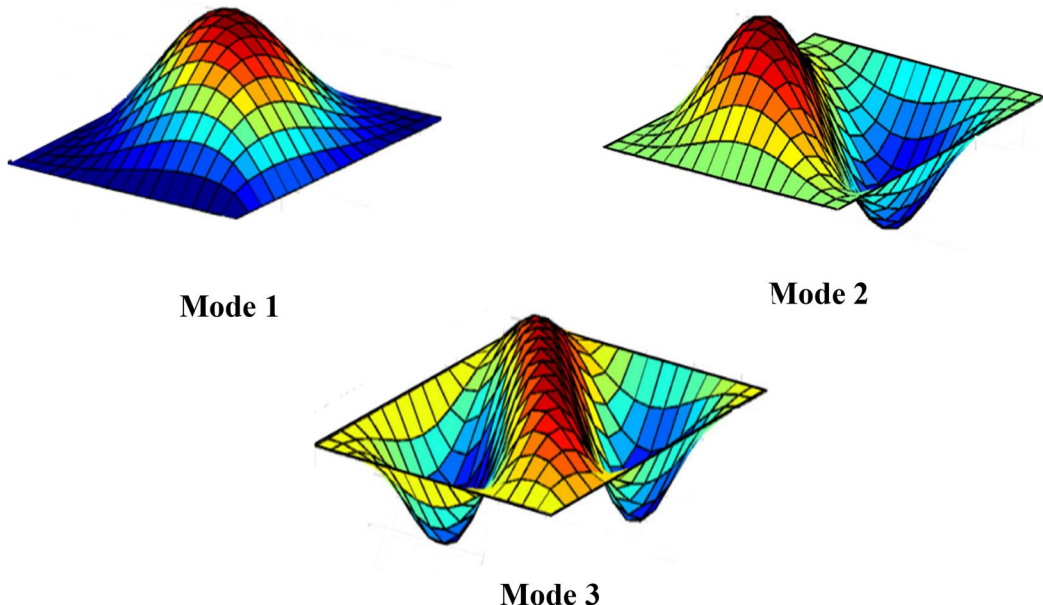


Figure 13. First three mode shapes of simply supported skew Al/ZrO₂-1 plate with ($p = 2$, $a/h = 10$, $\theta = 45^\circ$).

method by Katili et al. (2021) and the element-free kp-Ritz method by Zhao, Lee, and Liew (2009). This confirms the effectiveness and reliability of the current formulation for FG plates with complex geometries. The first three mode shapes of a simply supported FG skew plate are plotted in Fig. 13 for $a/h = 10$ and $p = 2$. According to Table 5, the dimensionless natural frequencies decrease as the gradient index p increases. This behavior can be attributed to a higher gradient index, which results in a lower volume fraction of ceramic material within the plate. Consequently, this reduction in ceramic content diminishes the overall bending stiffness, leading to lower natural frequencies. Furthermore, the boundary conditions have a significant impact on natural frequencies; the dimensionless frequency is minimized for simply supported boundary conditions and maximized for fully clamped conditions. This behavior arises because greater constraints at the edges enhance the bending stiffness of the plate, leading to increased vibrational responses.

4.2.3. Circular plate

To evaluate the reliability and robustness of the HSBQP20 element for analyzing FG plates with complex geometries, a clamped (CCCC) circular plate with varying thickness-radius ratios (h/R) is examined. The plate is composed of Material 1. The obtained results for the first three non-dimensional frequencies ($\bar{\omega}$), calculated using the mesh shown in Fig. 4(c), are presented in Table 6, while the corresponding mode shapes are depicted in Fig. 14 for $h/R = 0.1$.

The current results are in excellent agreement with the results from various methods, including FEM using ABAQUS (Tran, Ferreira, and Nguyen-Xuan 2013), semi-analytical solutions employing FSDT (Hosseini-Hashemi, Fadaee, and Es'haghi 2010b), and the numerical solution of Belounar, Boussem, and Tati (2022b) based on FSDT.

From the table, it can be observed that with a particular gradient index ($p = 1$), the dimensionless natural frequencies increase with the increase of the thickness-radius ratios (h/R). This is due to the fact that increasing the h/R generally leads to a greater contribution of bending stiffness. As the thickness becomes more significant relative to the radius, the overall rigidity of the plate increases, resulting in higher natural frequencies. Additionally, as the thickness increases in

Table 6. First three non-dimensional frequencies ($\bar{\omega}$) of a clamped circular plate composed of material 1 with a gradient index of ($p=1$).

		Clamped edge (CCCC)			
h/R	Mode	Present	(Belouanar, Boussem, and Tati 2022b)	(Tran, Ferreira, and Nguyen-Xuan 2013)	(Hosseini-Hashemi, Fadaee, and Es'haghi 2010b)
0.01	1	0.0238	0.0236	0.0234	0.0236
	2	0.0495	0.0493	0.0486	0.0491
	3	0.0811	0.0808	0.0798	0.0805
0.1	1	2.3067	2.3063	2.2888	2.3053
	2	4.7035	4.7030	4.6661	4.6934
	3	7.5142	7.5138	7.4808	7.5146
0.2	1	8.6572	8.6568	8.6403	8.6535
	2	16.7990	16.7986	16.7890	16.7666
	3	25.6635	25.6630	25.7661	25.6486

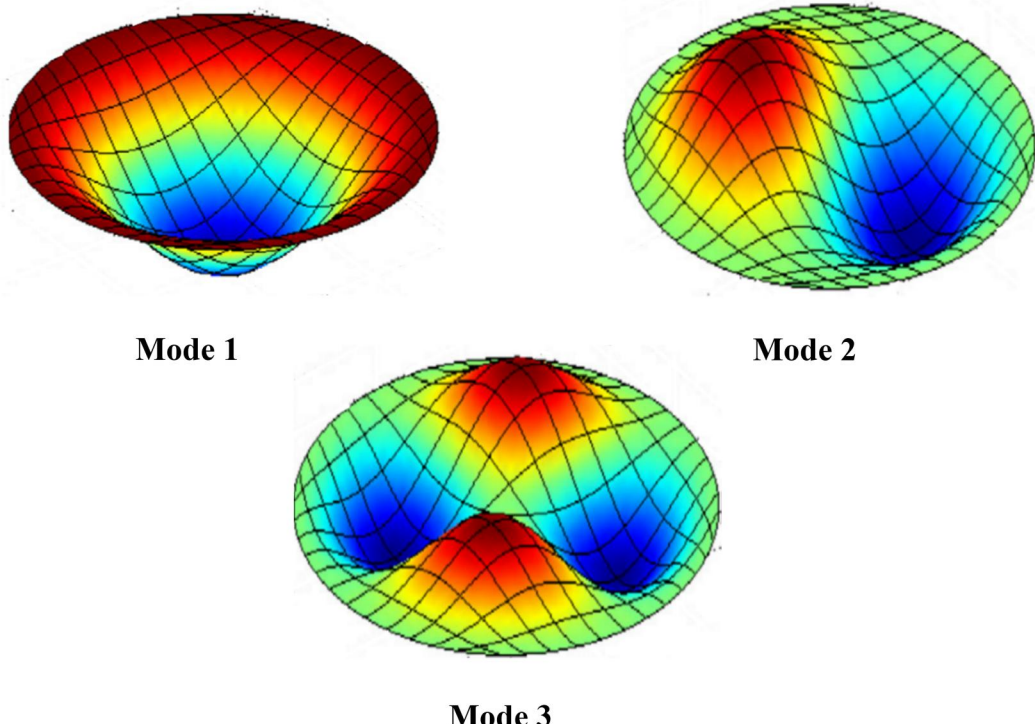


Figure 14. First three mode shapes of a CCCC circular Al/Al₂O₃ plate (h/R = 0.1).

relation to the radius, the inertial effects during vibration also become more significant. This shift in the balance between inertia and stiffness contributes to higher natural frequencies, as the plate exhibits greater resistance to motion.

5. Conclusion

The static and free vibration behavior of FG square, skew, and circular plates has been investigated using a HSBQP20 finite element model based on the strain approach and a simple HSDT. This model assumes a sinusoidal lateral shear stress distribution throughout the thickness of the plate and zero values at the free planes of the plate. The characteristics of FGM vary gradually with the volume fraction of their components in the thickness direction, following a power-law

function. The neutral surface concept is applied to eliminate stretching-bending coupling. Moreover, the total potential energy and Hamilton's principles are used to formulate the elementary stiffness and mass matrices. The efficiency of the novel HSBQP20 finite element for bending and vibrational behavior of FG plates has been evaluated with a number of tests taken from published literature. In addition, the effects of different parameters such as side-to-thickness ratio (a/h), power-law index (p), aspect ratio (b/a), geometric shape, and loading type with various boundary conditions on the static and free vibration behavior of FG plates are studied and discussed. Some of the effects can be listed as follows:

- The present element (HSBQP20) is both efficient and accurate in predicting the static and free vibration behaviors of FG plates.
- The current theory predicts excellent results for displacements and stresses when an FGM plate is subjected to static loading. The dimensionless displacement (\bar{w}) and normal stress ($\bar{\sigma}_x$) increase as p increases, while the in-plane shear stress ($\bar{\tau}_{xy}$) decreases due to the fact that an increase in the power-law index makes the FG plate more flexible.
- For both fully ceramic and fully metal plates, the stresses remain identical, reflecting the homogeneous nature of the material in both cases.
- The dimensionless displacement decreases as the side-to-thickness ratio (a/h) increases, whereas the dimensionless normal stress ($\bar{\sigma}_x$) and in-plane shear stress ($\bar{\tau}_{xy}$) increase.
- The proposed element is free from shear locking, ensuring stable performance across a range of length-to-thickness ratios in thin plates.
- The dimensionless natural frequencies increase with the side-to-thickness ratio and boundary constraints, while they decrease with increasing power-law index and aspect ratio.
- The results of this study demonstrate the effectiveness of the current element in modeling complex geometrical FG plates, including square, skew, and circular plates, with both clamped and simply supported boundary conditions, as well as for various gradient index values.

In perspective, the presented finite element model is a powerful numerical approach for the computation and simulation of FG plates. It will be extended in the future for the study of buckling analysis of FG plates and also for FG shell structures.

Disclosure statement

No potential competing interest was reported by the authors.

References

- Akavci, S. S., and A. H. Tanrikulu. 2015. "Static and Free Vibration Analysis of Functionally Graded Plates Based on a New Quasi-3D and 2D Shear Deformation Theories." *Composites Part B: Engineering* 83: 203–215. <https://doi.org/10.1016/j.compositesb.2015.08.043>
- Ashwell, D. G., and A. b Sabir. 1972. "A New Cylindrical Shell Finite Element Based on Simple Independent Strain Functions." *International Journal of Mechanical Sciences* 14 (3): 171–183. [https://doi.org/10.1016/0020-7403\(72\)90074-4](https://doi.org/10.1016/0020-7403(72)90074-4)
- Assas, T., M. Bourezane, and M. Chenafi. 2024. "Static, Free Vibration, and Buckling Analysis of Functionally Graded Plates Using the Strain-Based Finite Element Formulation." *Archive of Applied Mechanics* 94 (8): 2243–2267. <https://doi.org/10.1007/s00419-024-02635-0>
- Attia, A., A. T. Berrabah, F. Bourada, A. A. Bousahla, A. Tounsi, M. A. Salem, K. M. Khedher, and T. Cuong-Le. 2024. "Free Vibration Analysis of Thick Laminated Composite Shells Using Analytical and Finite Element Method." *Journal of Vibration Engineering & Technologies* 12: 1–18. <https://doi.org/10.1007/s42417-024-01322-2>
- Ba, Z., M. Wu, and J. Liang. 2020. "3D Dynamic Responses of a Multi-Layered Transversely Isotropic Saturated Half-Space under Concentrated Forces and Pore Pressure." *Applied Mathematical Modelling* 80: 859–878. <https://doi.org/10.1016/j.apm.2019.11.014>

- Batra, R. C., and J. Jin. 2005. "Natural Frequencies of a Functionally Graded Anisotropic Rectangular Plate." *Journal of Sound and Vibration* 282 (1–2): 509–516. <https://doi.org/10.1016/j.jsv.2004.03.068>
- Belabed, Z., A. Tounsi, M. Al-Osta, A. Tounsi, and H. L. Minh. 2024c. "On the Elastic Stability and Free Vibration Responses of Functionally Graded Porous Beams Resting on Winkler-Pasternak Foundations via Finite Element Computation." *Geomechanics and Engineering* 36 (2): 183–204. <https://doi.org/10.12989/gae.2024.36.2.183>
- Belabed, Z., A. Tounsi, A. A. Bousahla, A. Tounsi, M. Bourada, and M. A. Al-Osta. 2024b. "Free Vibration Analysis of Bi-Directional Functionally Graded Beams Using a Simple and Efficient Finite Element Model." *Structural Engineering and Mechanics* 90 (3): 233–245. <https://doi.org/10.12989/sem.2024.90.3.233>
- Belabed, Z., A. Tounsi, A. A. Bousahla, A. Tounsi, and M. Yaylaci. 2024a. "Accurate Free and Forced Vibration Behavior Prediction of Functionally Graded Sandwich Beams with Variable Cross-Section: A Finite Element Assessment." *Mechanics Based Design of Structures and Machines* 1–34. <https://doi.org/10.1080/15397734.2024.2337914>
- Belarbi, M. T., and A. Charif. 1999. "Développement D'un Nouvel Élément Hexaédrique Simple Basé Sur le Modèle en Déformation Pour L'étude Des Plaques Minces et Épaisses." *Revue Européenne des Éléments Finis* 8 (2): 135–157. <https://doi.org/10.1080/12506559.1999.10511361>
- Belarbi, M. T., and T. Maalem. 2005. "On Improved Rectangular Finite Element for Plane Linear Elasticity Analysis." *Revue Européenne des Éléments Finis* 14 (8): 985–997. <https://doi.org/10.3166/reef.14.985-997>
- Bellifa, H., K. H. Benrahou, L. Hadji, M. S. A. Houari, and A. Tounsi. 2016. "Bending and Free Vibration Analysis of Functionally Graded Plates Using a Simple Shear Deformation Theory and the Concept the Neutral Surface Position." *Journal of the Brazilian Society of Mechanical Sciences and Engineering* 38 (1): 265–275. <https://doi.org/10.1007/s40430-015-0354-0>
- Belounar, A., S. Benmebarek, and L. Belounar. 2020. "Strain Based Triangular Finite Element for Plate Bending Analysis." *Mechanics of Advanced Materials and Structures* 27 (8): 620–632. <https://doi.org/10.1080/15376494.2018.1488310>
- Belounar, A., S. Benmebarek, M. N. Houhou, and L. Belounar. 2019. "Static, Free Vibration, and Buckling Analysis of Plates Using Strain-Based Reissner-Mindlin Elements." *International Journal of Advanced Structural Engineering* 11 (2): 211–230. <https://doi.org/10.1007/s40091-019-0226-4>
- Belounar, A., S. Benmebarek, M. N. Houhou, and L. Belounar. 2020. "Free Vibration with Mindlin Plate Finite Element Based on the Strain Approach." *Journal of The Institution of Engineers (India): Series C* 101 (2): 331–346. <https://doi.org/10.1007/s40032-020-00555-w>
- Belounar, A., F. Boussem, M. N. Houhou, A. Tati, and L. Fortas. 2022a. "Strain-Based Finite Element Formulation for the Analysis of Functionally Graded Plates." *Archive of Applied Mechanics* 92 (7): 2061–2079. <https://doi.org/10.1007/s00419-022-02160-y>
- Belounar, A., F. Boussem, and A. Tati. 2022b. "A Novel C0 Strain-Based Finite Element for Free Vibration and Buckling Analyses of Functionally Graded Plates." *Journal of Vibration Engineering & Technologies* 11 (1): 281–300. <https://doi.org/10.1007/s42417-022-00577-x>
- Belounar, L., and M. Guenfoud. 2005. "A New Rectangular Finite Element Based on the Strain Approach for Plate Bending." *Thin-Walled Structures* 43 (1): 47–63. <https://doi.org/10.1016/j.tws.2004.08.003>
- Belounar, L., and K. Guerrache. 2014. "A New Strain Based Brick Element for Plate Bending." *Alexandria Engineering Journal* 53 (1): 95–105. <https://doi.org/10.1016/j.aej.2013.10.004>
- Benstrar, H., S. M. Chorfi, S. A. Belalia, A. Tounsi, M. H. Ghazwani, and A. Alnujaie. 2023. "Effect of Porosity Distribution on Free Vibration of Functionally Graded Sandwich Plate Using the P-Version of the Finite Element Method." *Structural Engineering and Mechanics* 88 (6): 551–567. <https://doi.org/10.12989/sem.2023.88.6.551>
- Boussem, F., and L. Belounar. 2020. "A Plate Bending Kirchhoff Element Based on Assumed Strain Functions." *Journal of Solid Mechanics* 12: 935–952. <https://doi.org/10.22034/jsm.2020.1901430.1601>
- Boussem, F., A. Belounar, and L. Belounar. 2022. "Assumed Strain Finite Element for Natural Frequencies of Bending Plates." *World Journal of Engineering* 19 (5): 620–631. <https://doi.org/10.1108/WJE-02-2021-0114>
- Cuong, B. M., A. Tounsi, D. V. Thom, N. T. H. Van, and P. V. Minh. 2024. "Finite Element Modelling for the Static Bending Response of Rotating FG-GPLRC Beams with Geometrical Imperfections in Thermal Mediums." *Journal of Structural Engineering* 33 (1): 91–102. <https://doi.org/10.12989/cac.2024.33.1.091>
- Damanpack, A., M. Bodaghi, H. Ghassemi, and M. Sayehbani. 2013. "Boundary Element Method Applied to the Bending Analysis of Thin Functionally Graded Plates." *Latin American Journal of Solids and Structures* 10 (3): 549–570. <https://doi.org/10.1590/S1679-78252013000300006>
- Demir, Ç., and Ö. Civalek. 2017. "A New Nonlocal FEM via Hermitian Cubic Shape Functions for Thermal Vibration of Nano Beams Surrounded by an Elastic Matrix." *Composite Structures* 168: 872–884. <https://doi.org/10.1016/j.compstruct.2017.02.091>
- Deng, K., L. Yang, Y. Lu, and S. Ma. 2024. "Multitype Chatter Detection via Multichannel Internal and External Signals in Robotic Milling." *Measurement* 229: 114417. <https://doi.org/10.1016/j.measurement.2024.114417>

- Do, V. T., V. V. Pham, and H. N. Nguyen. 2020. "On the Development of Refined Plate Theory for Static Bending Behavior of Functionally Graded Plates." *Mathematical Problems in Engineering* 2020: 1–13. <https://doi.org/10.1155/2020/2836763>
- Fukui, Y. 1991. "Fundamental Investigation of Functionally Gradient Material Manufacturing System Using Centrifugal Force." *JSME International Journal Series C-Mechanical Systems Machine Elements and Manufacturing* 34 (1): 144–148. <https://doi.org/10.1299/jsmec1988.34.144>
- Hosseini-Hashemi, S., M. Fadaee, and S. R. Atashipour. 2011. "Study on the Free Vibration of Thick Functionally Graded Rectangular Plates according to a New Exact Closed-Form Procedure." *Composite Structures* 93 (2): 722–735. <https://doi.org/10.1016/j.compstruct.2010.08.007>
- Hosseini-Hashemi, S., M. Fadaee, and M. Es'haghi. 2010b. "A Novel Approach for in-Plane/out-of-Plane Frequency Analysis of Functionally Graded Circular/Annular Plates." *International Journal of Mechanical Sciences* 52 (8): 1025–1035. <https://doi.org/10.1016/j.ijmecsci.2010.04.009>
- Hosseini-Hashemi, S., H. Rokni Damavandi Taher, H. Akhavan, and M. Omidi. 2010a. "Free Vibration of Functionally Graded Rectangular Plates Using First-Order Shear Deformation Plate Theory." *Applied Mathematical Modelling* 34 (5): 1276–1291. <https://doi.org/10.1016/j.apm.2009.08.008>
- Huang, H., C. Xue, W. Zhang, and M. Guo. 2022. "Torsion Design of CFRP-CFST Columns Using a Data-Driven Optimization Approach." *Engineering Structures* 251 (A): 113479. <https://doi.org/10.1016/j.engstruct.2021.113479>
- Jawaheri, R., and M. Eslami. 2002. "Buckling of Functionally Graded Plates Under in-Plane Compressive Loading." *ZAMM* 82 (4): 277–283. [https://doi.org/10.1002/1521-4001\(200204\)82:4<277::AID-ZAMM277>3.0.CO;2-Y](https://doi.org/10.1002/1521-4001(200204)82:4<277::AID-ZAMM277>3.0.CO;2-Y)
- Jin, G., Z. Su, S. Shi, T. Ye, and S. Gao. 2014. "Three-Dimensional Exact Solution for the Free Vibration of Arbitrarily Thick Functionally Graded Rectangular Plates with General Boundary Conditions." *Composite Structures* 108: 565–577. <https://doi.org/10.1016/j.compstruct.2013.09.051>
- Katili, I., J.-L. Batoz, I. J. Maknun, and A. M. Katili. 2021. "On Static and Free Vibration Analysis of FGM Plates Using an Efficient Quadrilateral Finite Element Based on DSPM." *Composite Structures* 261: 113514. <https://doi.org/10.1016/j.compstruct.2020.113514>
- Katiyar, S., A. Gupta, and A. Tounsi. 2022. "Microstructural/Geometric Imperfection Sensitivity on the Vibration Response of Geometrically Discontinuous bi-Directional Functionally Graded Plates (2D-FGPs) with Partial Supports by Using FEM." *Steel and Composite Structures* 45 (5): 621–640. <https://doi.org/10.12989/scs.2022.45.5.621>
- Lakhdar, Z., S. M. Chorfi, S. A. Belalia, K. M. Khedher, A. E. Alluqmani, A. Tounsi, and M. Yaylaci. 2024. "Free Vibration and Bending Analysis of Porous Bi-Directional FGM Sandwich Shell Using a TSDT p-Version Finite Element Method." *Acta Mechanica* 235 (6): 3657–3686. <https://doi.org/10.1007/s00707-024-03909-y>
- Leissa, A. W. 1973. "The Free Vibration of Rectangular Plates." *Journal of Sound and Vibration* 31 (3): 257–293. [https://doi.org/10.1016/S0022-460X\(73\)80371-2](https://doi.org/10.1016/S0022-460X(73)80371-2)
- Li, J., Z. Wang, S. Zhang, Y. Lin, L. Wang, C. Sun, and J. Tan. 2023. "A Novelty Mandrel Supported Thin-Wall Tube Bending Cross-Section Quality Analysis: A Diameter-Adjustable Multi-Point Contact Mandrel." *The International Journal of Advanced Manufacturing Technology* 124 (11-12): 4615–4637. <https://doi.org/10.1007/s00170-023-10838-y>
- Liu, K., S. Zong, Y. Li, Z. Wang, Z. Hu, and Z. Wang. 2022. "Structural Response of the U-Type Corrugated Core Sandwich Panel Used in Ship Structures under the Lateral Quasi-Static Compression Load." *Marine Structures* 84: 103198. <https://doi.org/10.1016/j.marstruc.2022.103198>
- Mantari, J. L., E. V. Granados, and C. Guedes Soares. 2014. "Vibrational Analysis of Advanced Composite Plates Resting on Elastic Foundation." *Composites Part B: Engineering* 66: 407–419. <https://doi.org/10.1016/j.compositesb.2014.05.026>
- Matsunaga, H. 2008. "Free Vibration and Stability of Functionally Graded Plates according to a 2-D Higher-Order Deformation Theory." *Composite Structures* 82 (4): 499–512. <https://doi.org/10.1016/j.compstruct.2007.01.030>
- Mechab, I., B. Mechab, and S. Benissa. 2013. "Static and Dynamic Analysis of Functionally Graded Plates Using Four-Variable Refined Plate Theory by the New Function." *Composites Part B: Engineering* 45 (1): 748–757. <https://doi.org/10.1016/j.compositesb.2012.07.015>
- Meftah, S. A., S. M. Aldosari, A. Tounsi, T. Cuong-Le, K. M. Khedher, and A. E. Alluqmani. 2024. "Simplified Homogenization Technique for Nonlinear Finite Element Analysis of in-Plane Loaded Masonry Walls." *Engineering Structures* 306: 117822. <https://doi.org/10.1016/j.engstruct.2024.117822>
- Mesbah, A., Z. Belabed, K. Amara, A. Tounsi, A. A. Bousahla, and F. Bourada. 2023. "Formulation and Evaluation of a Finite Element Model for Free Vibration and Buckling Behaviors of Functionally Graded Porous (FGP) Beams." *Structural Engineering and Mechanics* 86 (3): 291–309. <https://doi.org/10.12989/sem.2023.86.3.291>
- Messai, A., L. Belounar, and T. Merzouki. 2019. "Static and Free Vibration of Plates with a Strain Based Brick Element." *European Journal of Computational Mechanics* 99 (1): 1–21. <https://doi.org/10.1080/17797179.2018.1560845>
- Mindlin, R. D. 1951. "Influence of Rotatory Inertia and Shear on Flexural Motions of Isotropic, Elastic Plates." *Journal of Applied Mechanics* 18 (1): 31–38. <https://doi.org/10.1115/1.4010217>

- Mohammadi, M., A. R. Saidi, and E. Jomehzadeh. 2010. "Levy Solution for Buckling Analysis of Functionally Graded Rectangular Plates." *Applied Composite Materials* 17 (2): 81–93. <https://doi.org/10.1007/s10443-009-9100-z>
- Morley, L. S. D. 1963. *Skew Plates and Structures*. Oxford: Pergamon Press.
- Nguyen, V.-H., T.-K. Nguyen, H.-T. Thai, and T. P. Vo. 2014. "A New Inverse Trigonometric Shear Deformation Theory for Isotropic and Functionally Graded Sandwich Plates." *Composites Part B: Engineering* 66: 233–246. <https://doi.org/10.1016/j.compositesb.2014.05.012>
- Praveen, G. N., and J. Reddy. 1998. "Nonlinear Transient Thermoelastic Analysis of Functionally Graded Ceramic-Metal Plates." *International Journal of Solids and Structures* 35 (33): 4457–4476. [https://doi.org/10.1016/S0020-7683\(97\)00253-9](https://doi.org/10.1016/S0020-7683(97)00253-9)
- Rebiai, C., and L. Belounar. 2013. "A New Strain Based Rectangular Finite Element with Drilling Rotation for Linear and Nonlinear Analysis." *Archives of Civil and Mechanical Engineering* 13 (1): 72–81. <https://doi.org/10.1016/j.acme.2012.10.001>
- Reddy, J. 2000. "Analysis of Functionally Graded Plates." *International Journal for Numerical Methods in Engineering* 47 (1-3): 663–684. [https://doi.org/10.1002/\(SICI\)1097-0207\(20000110/30\)47:1/3<663::AID-NME787>3.0.CO;2-8](https://doi.org/10.1002/(SICI)1097-0207(20000110/30)47:1/3<663::AID-NME787>3.0.CO;2-8)
- Sabir, A. B. 1985. "A Rectangular and Triangular Plane Elasticity Element with Drilling Degrees of Freedom." In *Proceedings of the 2nd International Conference on Variational Methods in Engineering*. Southampton University, Springer-Verlag, Berlin, 17–25.
- Sabir, A. B., and A. Sfendji. 1995. "Triangular and Rectangular Plane Elasticity Finite Elements." *Thin-Walled Structures* 21 (3): 225–232. [https://doi.org/10.1016/0263-8231\(94\)00002-H](https://doi.org/10.1016/0263-8231(94)00002-H)
- Sadgui, A., and A. Tati. 2022. "A Novel Trigonometric Shear Deformation Theory for the Buckling and Free Vibration Analysis of Functionally Graded Plates." *Mechanics of Advanced Materials and Structures* 29 (27): 6648–6663. <https://doi.org/10.1080/15376494.2021.1983679>
- Sekban, D. M., E. U. Yayılcı, M. E. Özdemir, M. Yayılcı, and A. Tounsi. 2024. "Investigating Formability Behavior of Friction Stir-Welded High-Strength Shipbuilding Steel Using Experimental, Finite Element, and Artificial Neural Network Methods." *Journal of Materials Engineering and Performance*. <https://doi.org/10.1007/s11665-024-09501-8>
- Su, Y., P. M. Iyela, J. Zhu, X. Chao, S. Kang, and X. Long. 2024. "A Voronoi-Based Gaussian Smoothing Algorithm for Efficiently Generating RVEs of Multi-Phase Composites with Graded Aggregates and Random Pores." *Materials & Design* 244: 113159. <https://doi.org/10.1016/j.matdes.2024.113159>
- Talha, M., and B. N. Singh. 2010. "Static Response and Free Vibration Analysis of FGM Plates Using Higher Order Shear Deformation Theory." *Applied Mathematical Modelling* 34 (12): 3991–4011. <https://doi.org/10.1016/j.apm.2010.03.034>
- Tati, A. 2021a. "Finite Element Analysis of Thermal and Mechanical Buckling Behavior of Functionally Graded Plates." *Archive of Applied Mechanics* 91 (11): 4571–4587. <https://doi.org/10.1007/s00419-021-02025-w>
- Tati, A. 2021b. "A Five Unknowns High Order Shear Deformation Finite Element Model for Functionally Graded Plates Bending Behavior Analysis." *Journal of the Brazilian Society of Mechanical Sciences and Engineering* 43 (1): 1–14. <https://doi.org/10.1007/s40430-020-02736-1>
- Tati, A., A. Belounar, and A. Sadgui. 2024. "Bending and Free Vibration Analysis of FG Circular Plates Using a Five Unknown High Order Shear Deformation Theory." *Mechanics Based Design of Structures and Machines* 52 (10): 8116–8140. <https://doi.org/10.1080/15397734.2024.2315173>
- Thai, H.-T., and D.-H. Choi. 2013a. "A Simple First-Order Shear Deformation Theory for Laminated Composite Plates." *Composite Structures* 106: 754–763. <https://doi.org/10.1016/j.compstruct.2013.06.013>
- Thai, H.-T., and D.-H. Choi. 2013b. "A Simple First-Order Shear Deformation Theory for the Bending and Free Vibration Analysis of Functionally Graded Plates." *Composite Structures* 101: 332–340. <https://doi.org/10.1016/j.compstruct.2013.02.019>
- Thai, H.-T., T.-K. Nguyen, T. P. Vo, and J. Lee. 2014. "Analysis of Functionally Graded Sandwich Plates Using a New First-Order Shear Deformation Theory." *European Journal of Mechanics – A/Solids* 45: 211–225. <https://doi.org/10.1016/j.euromechsol.2013.12.008>
- Tian, R., M. Wang, Y. Zhang, X. Jing, and X. Zhang. 2024. "A Concave X-Shaped Structure Supported by Variable Pitch Springs for Low-Frequency Vibration Isolation." *Mechanical Systems and Signal Processing* 218: 111587. <https://doi.org/10.1016/j.ymssp.2024.111587>
- Tien, D. M., D. V. Thom, N. T. H. Van, A. Tounsi, P. V. Minh, and D. N. Mai. 2023. "Buckling and Forced Oscillation of Organic Nanoplates Taking the Structural Drag Coefficient into account." *Computers and Concrete* 32 (6): 553–565. <https://doi.org/10.12989/cac.2023.32.6.553>
- Timoshenko, S., and S. Woinowsky-Krieger. 1959. *Theory of Plates and Shells*. Vol. 2. New York: McGraw-Hill.
- Tran, L. V., A. J. M. Ferreira, and H. Nguyen-Xuan. 2013. "Isogeometric Analysis of Functionally Graded Plates Using Higher-Order Shear Deformation Theory." *Composites Part B: Engineering* 51: 368–383. <https://doi.org/10.1016/j.compositesb.2013.02.045>

- Wang, C., Z. Wang, S. Zhang, X. Liu, and J. Tan. 2023. "Reinforced Quantum-Behaved Particle Swarm-Optimized Neural Network for Cross-Sectional Distortion Prediction of Novel Variable-Diameter-Die-Formed Metal Bent Tubes." *Journal of Computational Design and Engineering* 10 (3): 1060–1079. <https://doi.org/10.1093/jcde/qwad037>
- Xia, L., R. Wang, G. Chen, K. Asemi, and A. Tounsi. 2023. "The Finite Element Method for Dynamics of FG Porous Truncated Conical Panels Reinforced with Graphene Platelets Based on the 3-D Elasticity." *Advances in Nano Research* 14 (4): 375–389. <https://doi.org/10.12989/anr.2023.14.4.375>
- Yang, M., C. Cai, D. Wang, Q. Wu, Z. Liu, and Y. Wang. 2024. "Symmetric Differential Demodulation-Based Heterodyne Laser Interferometry Used for Wide Frequency-Band Vibration Calibration." *IEEE Transactions on Industrial Electronics* 71 (7): 8129–8137. <https://doi.org/10.1109/TIE.2023.3299015>
- Ye, W., L. Jun, Z. Jing, L. Fan, and Gao, Y. 2021. "A New Semi-Analytical Solution of Bending, Buckling and Free Vibration of Functionally Graded Plates Using Scaled Boundary Finite Element Method." *Thin-Walled Structures* 163: 107776. <https://doi.org/10.1016/j.tws.2021.107776>
- Yuan, X., W. Wang, H. Pang, and L. Zhang. 2024. "Analysis of Vibration Characteristics of Electro-Hydraulic Driven 3-UPS/S Parallel Stabilization Platform." *Chinese Journal of Mechanical Engineering* 37 (1): 96. <https://doi.org/10.1186/s10033-024-01074-w>
- Zenkour, A. M. 2006. "Generalized Shear Deformation Theory for Bending Analysis of Functionally Graded Plates." *Applied Mathematical Modelling* 30 (1): 67–84. <https://doi.org/10.1016/j.apm.2005.03.009>
- Zhang, W., S. Kang, X. Liu, B. Lin, and Y. Huang. 2023. "Experimental Study of a Composite Beam Externally Bonded with a Carbon Fiber-Reinforced Plastic Plate." *Journal of Building Engineering* 71: 106522. <https://doi.org/10.1016/j.jobe.2023.106522>
- Zhang, J., and C. Zhang. 2023. "Using Viscoelastic Materials to Mitigate Earthquake-Induced Pounding between Adjacent Frames with Unequal Height considering Soil-Structure Interactions." *Soil Dynamics and Earthquake Engineering* 172: 107988. <https://doi.org/10.1016/j.soildyn.2023.107988>
- Zhao, X., Y. Y. Lee, and K. M. Liew. 2009. "Free Vibration Analysis of Functionally Graded Plates Using the Element-Free kp-Ritz Method." *Journal of Sound and Vibration* 319 (3–5): 918–939. <https://doi.org/10.1016/j.jsv.2008.06.025>

Appendix

The membrane strains $\{\varepsilon_m\}$ indicated in Eq. (42) satisfied the compatibility conditions as follows:

$$\frac{\partial^2 \varepsilon_x}{\partial y^2} + \frac{\partial^2 \varepsilon_y}{\partial x^2} - \frac{\partial^2 \gamma_{xy}}{\partial x \partial y} = 0 \quad (\text{A1})$$

The shear strains and curvatures (γ_{xz} , γ_{yz} , κ_x , κ_y , κ_{xy}) given in Eqs. (43)–(44) are satisfy by the following compatibility equations:

$$\begin{aligned} \frac{\partial^2 \kappa_x}{\partial y^2} + \frac{\partial^2 \kappa_y}{\partial x^2} &= \frac{\partial^2 \kappa_{xy}}{\partial x \partial y} \\ \frac{\partial^2 \gamma_{xz}}{\partial x \partial y} - \frac{\partial^2 \gamma_{yz}}{\partial x^2} + \frac{\partial \kappa_{xy}}{\partial x} &= 2 \frac{\partial \kappa_x}{\partial y} \\ \frac{\partial^2 \gamma_{yz}}{\partial x \partial y} - \frac{\partial^2 \gamma_{xz}}{\partial y^2} + \frac{\partial \kappa_{xy}}{\partial y} &= 2 \frac{\partial \kappa_y}{\partial x} \end{aligned} \quad (\text{A2})$$

Symbols

a,b	length and width of the plate
[\mathbf{B}_m], [\mathbf{B}_b], [\mathbf{B}_s]	membrane, bending, and Shear strain-displacement relationship matrices
C	enhancement factor.
[\mathbf{D}_m], [\mathbf{D}_s], [\mathbf{D}_b]	membrane, shear and bending matrix, respectively
e_N	distance between the neutral surface and the middle surface of the plate
E	Young's modulus
E_c, E_m	Young's modulus of metal and ceramic, respectively
$f(z)$	shear function
{ \mathbf{F}^e }	nodal load vector
{ \mathbf{F} }	structural load vector

h	thickness of plate
$[H]$	transformation matrix
I_0, I_2	the moments of inertia.
$\{\kappa\}$	curvatures vector
$[K^e]$	elementary stiffness matrix
$[K]$	structural stiffness matrix
$[L_m], [L_b], [L_s]$	membrane, bending, and the transverse shear strains matrices
M_x, M_y, M_{xy}	moment resultants
$[M^e]$	element mass matrix
$[M]$	structural mass matrix
$\{N\}$	total in-plane forces
N_x, N_y, N_{xy}	normal stress resultants
p	power-law index p ,
$[P_m]$	matrix polynomial of the displacement field for the membrane element
$[P_b]$	matrix polynomial of the displacement field for the bending element
q_v	distributed load
t	time
T	kinetic energy
$\{T\}$	shear forces
U	the strain potential energy
u, v	in-plane displacements vector components
u_0, v_0	in-plane displacements on the neutral surface of the plate
w	transverse displacement
W	the external forces work
w_0	lateral displacement on the mid-plane of the plate
(β_x, β_y)	normal rotations in the yz -plane and xz -plane
$\{\epsilon^0\}$	membrane strain vector
$\{\gamma_z^0\}$	shear strain vector
σ_x, σ_y	normal stresses
τ_{xy}	in-plane shear stress
σ_z	transverse normal stress
ν	Poisson's ratio
π	the total potential energy
ρ	mass density
Ω	surface of the plate.
ω	natural frequency
δ^e	vector of elemental nodal displacements